Geochemistry, Geophysics, Geosystems®

AGU ADVANCING EARTH AND SPACE SCIENCES

RESEARCH ARTICLE
10.1029/2024GC012123

Investigating the Lid Effect on the Generation of Ocean Island Basalts: 2. Geodynamical Simulations

Shihao Jiang[1], Thomas Duvernay[1], Mark J. Hoggard[1], Rhys Hawkins[1], Ian H. Campbell[1], and D. Rhodri Davies[1]

[1]Research School of Earth Sciences, Australian National University, Canberra, ACT, Australia

Key Points:

- Plume simulations support the lithospheric lid and melt-flux filter effects inferred from ocean island basalt (OIB) geochemistry
- Local melts across the melting domain of a single-lithology plume can reproduce observed spread in trace elements from individual islands
- Primitive mantle lacks sufficient rare earth elements to match OIB compositions, requiring input from recycled materials in the OIB source

Supporting Information:

Supporting Information may be found in the online version of this article.

Correspondence to:

S. Jiang,
shihao.jiang1@anu.edu.au

Citation:

Jiang, S., Duvernay, T., Hoggard, M. J., Hawkins, R., Campbell, I. H., & Davies, D. R. (2025). Investigating the lid effect on the generation of ocean island basalts: 2. Geodynamical simulations. *Geochemistry, Geophysics, Geosystems*, *26*, e2024GC012123. https://doi.org/10.1029/2024GC012123

Received 17 DEC 2024
Accepted 19 FEB 2025

Author Contributions:

Conceptualization: Shihao Jiang, Thomas Duvernay, Mark J. Hoggard, Ian H. Campbell, D. Rhodri Davies
Data curation: Shihao Jiang, Rhys Hawkins
Formal analysis: Shihao Jiang, Rhys Hawkins, Ian H. Campbell, D. Rhodri Davies
Funding acquisition: Rhys Hawkins, D. Rhodri Davies
Investigation: Shihao Jiang, Thomas Duvernay, Mark J. Hoggard, Ian H. Campbell, D. Rhodri Davies

Abstract The concept that oceanic lithosphere mechanically limits upwelling and decompression melting of mantle plumes is known as the *lid effect* and is backed up by observations of ocean island basalt (OIB) geochemistry. Nevertheless, in a recent companion study on OIB geochemistry, several additional factors were identified that further influence OIB compositions including a *melt-flux filter*, whereby plumes with small melt fluxes progressively fail to be sampled in regions of thicker lithosphere. Here, we use 3-D coupled geochemical-geodynamical simulations of decompression melting in a single-lithology mantle plume to predict basalt trace element concentrations for comparison with observations. In addition to supporting the role of the *lid effect* and *melt-flux filter*, our models demonstrate that, if it is possible to extract local melts from across the melting domain without complete homogenization, much of the spread in OIB geochemistry observed at individual ocean islands can be reproduced using a single source lithology. Nevertheless, we also find that an OIB source composed solely of primitive mantle contains insufficient rare earth element enrichment, necessitating a recycled crustal component.

Plain Language Summary Many of the world's volcanic islands are formed by mantle plumes—regions of hot, buoyant rock that rise from deep within Earth's mantle. As plumes ascend to the upper mantle, they partially melt due to decreasing pressure. However, their ascent is limited by the lithosphere—Earth's cold, rigid outer shell—which controls the melting pressure and influences the composition of magma produced. In our previous work, we quantified how lithospheric thickness affects the geochemistry of ocean island basalts—volcanic rocks that often erupt far from tectonic boundaries. Building on those results, here we use numerical simulations to model melting in mantle plumes and compare results with observations. Our study shows that, under older and thicker oceanic lithosphere, only the hottest plumes generate enough magma to create volcanic seamounts or islands. Furthermore, the observed diversity of OIB compositions in the same volcanic system can be reproduced without necessarily invoking multiple different plume lithologies. Finally, our results suggest that recycled components contribute to the mantle source of OIBs. This outcome suggests that material subducted into Earth's mantle millions of years ago can resurface in volcanic eruptions, offering a glimpse into the planet's deep recycling processes.

1. Introduction

A significant portion of Earth's intra-plate volcanic activity marks the surface expression of mantle plumes: hot, buoyant regions of rock that rise from the core-mantle boundary (CMB) toward the surface, undergoing decompression melting in the uppermost mantle (e.g., Davies & Davies, 2009; Davies, Goes, & Sambridge, 2015; French & Romanowicz, 2015; Griffiths & Campbell, 1990, 1991; Koppers et al., 2021; Morgan, 1971; Sleep, 2006). Voluminous plume heads drive the formation of large igneous provinces through massive volcanic activity, while plume tails generate smaller but longer-lasting volcanic chains, such as those associated with OIBs (e.g., Campbell et al., 1989; Duncan & Richards, 1991; M. A. Richards et al., 1989; R. White & McKenzie, 1989).

Due to its mechanical strength, the lithosphere—Earth's rigid outermost shell—is difficult to deform, even under the influence of mantle plumes (e.g., Burov & Gerya, 2014; Burov et al., 2007; Campbell, 2007; Davies, Rawlinson, et al., 2015). The base of the lithosphere acts as a barrier to plume ascent, with its thickness controlling the pressure at which decompression melting ceases—a phenomenon known as the *lid effect* (e.g., Humphreys & Niu, 2009; Niu et al., 2011). This process has been investigated at both regional and global scales, with growing evidence that OIBs erupting onto thicker lithosphere bear geochemical signatures indicative of higher average

Methodology: Shihao Jiang, Thomas Duvernay, Rhys Hawkins, Ian H. Campbell, D. Rhodri Davies
Project administration: D. Rhodri Davies
Resources: Mark J. Hoggard, D. Rhodri Davies
Software: Shihao Jiang, Thomas Duvernay, D. Rhodri Davies
Supervision: Mark J. Hoggard, Ian H. Campbell, D. Rhodri Davies
Validation: Shihao Jiang, Thomas Duvernay, Mark J. Hoggard
Visualization: Shihao Jiang
Writing – original draft: Shihao Jiang
Writing – review & editing: Shihao Jiang, Thomas Duvernay, Mark J. Hoggard, Ian H. Campbell, D. Rhodri Davies

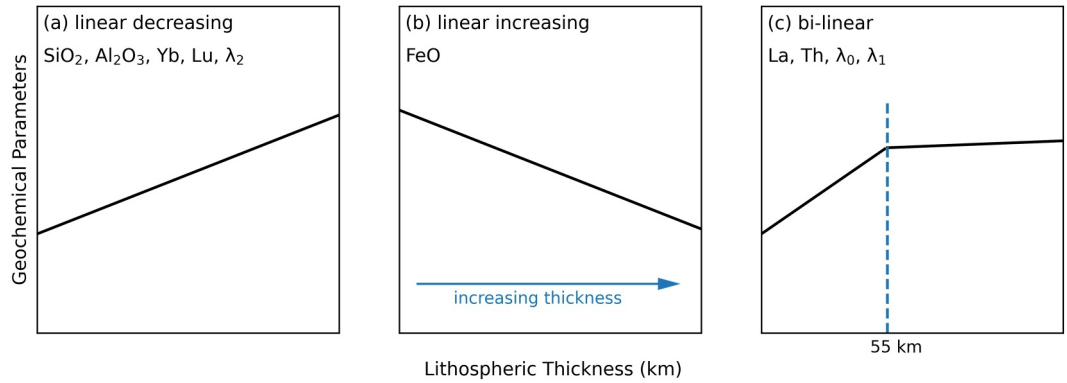

Figure 1. Schematic summary of observed relationship between geochemical variables in OIBs and lithospheric thickness. (a) SiO_2, Al_2O_3, Yb, Lu, and λ_2 linearly decrease with increasing lithospheric thickness. Note that the slopes for Yb and Lu are consistently low, often near zero, with trends that can sometimes be considered constant. (b) FeO, linearly increases with increasing lithospheric thickness. (c) La, Th, λ_0, and λ_0 first increase with increasing lithospheric thickness before stabilizing beyond a thickness of ~55 km (denoted by the dashed vertical line).

melting pressures (e.g., Dasgupta et al., 2010; Ellam, 1992; Gibson & Geist, 2010; Hole & Millett, 2016; Niu, 2021; Watson & McKenzie, 1991).

In a companion study (Jiang et al., 2024), we employed a probabilistic Bayesian framework to quantitatively evaluate the observed relationship between OIB geochemistry and lithospheric thickness. For basalt compositions, we compiled a database of geochemical analyses that were filtered and corrected for the effects of fractionation. For lithospheric thickness estimates (treated as a proxy for thickness of the mechanical boundary layer), we used recent theoretical models of oceanic cooling and observational constraints derived from surface-wave tomography (F. D. Richards, Hoggard, Crosby, et al., 2020; F. D. Richards, Hoggard, White, & Ghelichkhan, 2020; Hoggard, Czarnota, et al., 2020), both of which define the lithosphere-asthenosphere boundary (LAB) via the depth of the 1175°C isotherm. This approach provided robust evidence for a correlation between OIB geochemistry and lithospheric thickness, consistent with the *lid effect* hypothesis.

A number of different geochemical variables were assessed, such as major and trace element concentrations and the λ rare earth element (REE) coefficients of O'Neill (2016), where λ_0 corresponds to the logarithmic mean REE concentration, λ_1 is the light rare earth element (LREE) enrichment relative to heavy rare earth element (HREE), and λ_2 is the curvature of REE patterns. Each variable was found to exhibit different sensitivities to lithospheric thickness (Figure 1). Some, such as SiO_2, Al_2O_3, FeO, Lu, Yb, and λ_2, showed constant or linear trends, indicating either no apparent sensitivity or a straightforward *lid effect*. In contrast, others, including La, Th, λ_0, and λ_1, displayed bi-linear trends with a clear inflection point at a lithospheric thickness of ~55 km, suggesting a more nuanced *lid effect*. In particular, bi-linear trends were identified for highly incompatible elements including Th and La, with concentrations increasing alongside lithospheric thickness up to ~55 km, after which they remain nearly constant. This behavior led to the following interpretations:

1. The *lid effect*. For lithospheric thicknesses less than ~55 km, OIBs exhibit a decline in the average degree of melting (F) and an increase in the average melting pressure with increasing lithospheric thickness (McKenzie & Bickle, 1988). In this regime, the *lid effect* dominates, while plume excess temperatures and source lithologies play a secondary role in controlling melt production.
2. The *melt-flux filter*. For lithospheric thicknesses greater than ~55 km, the degree of melting (F) appears to stabilize despite increasing lithospheric thickness. Since theoretical models predict a continuous decrease in F with increasing thickness, this effect must be counteracted by a sampling bias that favors plumes with higher melt fluxes that generate sufficient melt volumes for extraction through thick lithosphere. Such an effect could arise from preferential sampling of hotter plumes beneath thicker lithosphere, a process we previously termed the *temperature effect*.
3. *Plume-driven lithospheric thinning*. For lithospheric thicknesses exceeding ~55 km, plume-driven thinning or thermal rejuvenation could further contribute to the stabilization of F (Ballmer et al., 2011; Crough, 1978; Watson & McKenzie, 1991), complementing the effects of the melt-flux filter. Supporting evidence for this

process comes from observed discrepancies between the seismically derived lithospheric thickness at the sites of major hotspots and the thickness that would be expected from empirical cooling models that do not account for plume-induced thinning.

A further consideration involves the factors driving the observed variation in OIB compositions within individual ocean islands. Isotopic signatures provide strong evidence for a multi-lithology plume source incorporating recycled oceanic material (e.g., Chauvel et al., 2008; Halldórsson et al., 2016; Jackson et al., 2007; Sobolev et al., 2007; Soderman et al., 2024; Weaver, 1991), and this mixture of sources has been invoked as a significant contributor to OIB compositional variability. Nevertheless, Jiang et al. (2024) proposed that much of this variability could instead potentially be explained by considering the melting dynamics of a single-lithology plume. Specifically, variations in the composition of primary magmas generated in different regions of the melting domain could account for the major and trace element diversity observed in OIBs, provided that melts are extracted to the surface without undergoing complete homogenization or equilibration. Jiang et al. (2024) also acknowledged that magma chamber processes, such as recharge and mixing, likely further shape the compositional spectrum (e.g., Borisova et al., 2017; Gleeson & Gibson, 2019).

This study builds on our previous work (Jiang et al., 2024) by utilizing coupled geochemical and geodynamical simulations of peridotitic decompression melting in mantle plumes. Our primary aim is to evaluate the effectiveness of the key interpretations outlined above in accounting for observed trends in OIB geochemistry. While numerous studies have explored the dynamics of mantle plumes (e.g., Ballmer et al., 2011; Dannberg & Sobolev, 2015; Davies & Davies, 2009; Farnetani & Hofmann, 2010; Jones et al., 2017; Koppers et al., 2021; Lin & van Keken, 2005; Wang & Li, 2021), assessed how they sample mantle heterogeneity (e.g., Brandenburg et al., 2008; Farnetani et al., 2018; Jones et al., 2017, 2019), and investigated how plumes drive surface magmatism (e.g., Ballmer et al., 2011; Duvernay et al., 2022; Jones et al., 2017; Ribe & Christensen, 1999; Wang & Li, 2021), few have systematically connected melting region characteristics and magma composition to lithospheric thickness and plume excess temperature. To address this knowledge gap, we establish the following objectives:

1. To predict trace element trends as a function of lithospheric thickness and compare them with observational data;
2. To quantify the impact of plume excess temperature and associated *melt-flux filter* beneath thicker lithosphere;
3. To simulate the effects of plume-induced thinning or thermal rejuvenation of the overlying lithosphere;
4. To analyze the compositional variability in instantaneous magma compositions within a single-lithology plume;
5. To assess the requirement for different lithologies in the OIB source.

By addressing these objectives, we aim to provide new insights into the geochemical evolution of OIBs and the interplay between mantle plume dynamics, lithospheric structure, and melt generation processes. The paper is organized as follows: Section 2 outlines our numerical approach, including the mantle plume simulation setup and the methods used to model partial melting and track melt composition. In Section 3, we present results from a reference case, analyze the sensitivity of melt diagnostics to variations in excess temperature and lithospheric thickness across a broad parameter space, and compare synthetically predicted geochemical trends with observed OIB data. Finally, in Section 4, we use insights from our geodynamical simulations to evaluate the validity of the interpretations introduced above.

2. Methods

We examine the dynamics of melting in upwelling mantle plumes using coupled geochemical-geodynamical simulations. We employ Fluidity, a combined finite element, control-volume computational modeling framework (e.g., Davies et al., 2011; S. C. Kramer et al., 2012), in which anisotropic, unstructured meshes are adapted in parallel and on the fly to enhance resolution in dynamically significant areas (e.g., Davies et al., 2007). Fluidity has been extensively validated for mantle convection simulations against analytical and empirical benchmark solutions (e.g., Davies et al., 2011; S. C. Kramer et al., 2012; Le Voci et al., 2014; Tosi et al., 2015; S. C. Kramer et al., 2021). Here, we couple Fluidity to BDD21—a numerical framework that calculates peridotite melting, melt chemistry, and magmatic differentiation (Ball et al., 2022; Duvernay et al., 2024)—to determine how plume excess temperature and overlying lithospheric thickness modulate the geochemical characteristics of

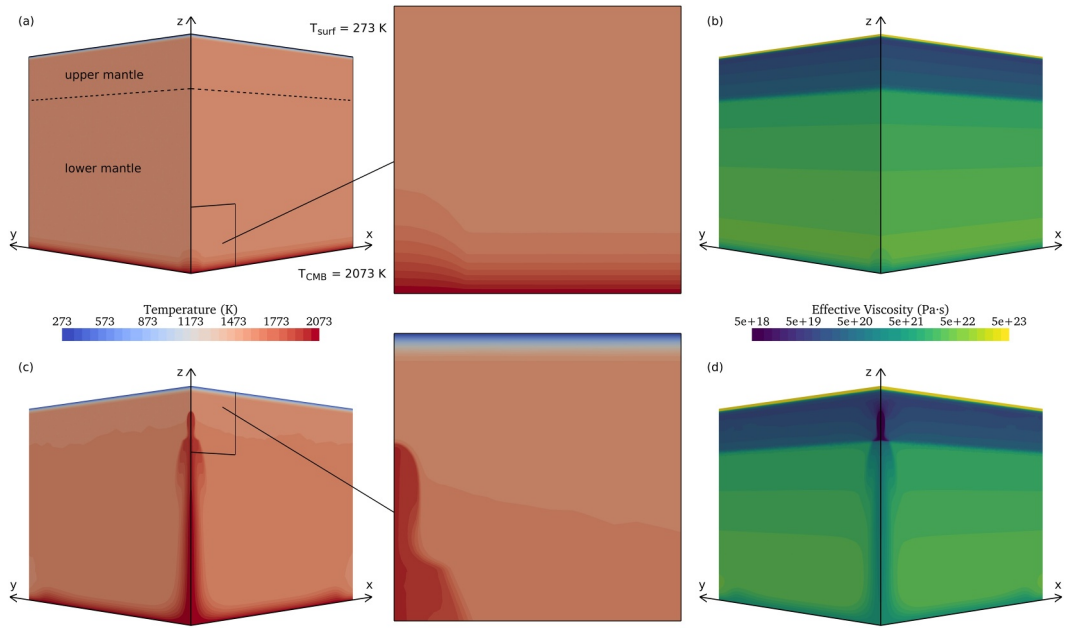

Figure 2. Model setup for the reference simulation ΔT500_LT56 with $T_{CMB} = 2073$ K (i.e., 500 K excess temperature at core-mantle boundary with respect to ambient mantle). (a) 3-D perspective view showing initial temperature field on the two symmetric boundary planes (i.e., on $x = 0$ and $y = 0$). The black dashed line marks the upper-to-lower mantle transition at 660 km beneath the surface, and the small black box shows the location of the 800 km × 800 km zoomed-in region. (b) Same as (a) for the initial effective viscosity field. (c–d) Snapshots of the temperature and effective viscosity fields when the plume enters the upper mantle and the lithospheric thickness is reset according to Equation 4 with $t_{lt} = 20$ Myr.

OIBs. We systematically explore the sensitivity of our results across a wide parameter space, focusing on the resulting degree of melting, melting rate, volumetric melt production rate, and trace element concentrations.

2.1. Simulation Setup

Within a 3-D Cartesian domain of dimensions $3470 \times 3470 \times 2890$ km ($x : y : z$) and adaptive mesh size between 2.5 and 300 km, we solve the incompressible mantle convection equations, formulated under the Boussinesq approximation, governing conservation of mass, momentum, and energy

$$\nabla \cdot \boldsymbol{u} = 0, \tag{1}$$

$$\nabla \cdot \boldsymbol{\tau} = \nabla p - \rho \boldsymbol{g}, \tag{2}$$

$$\frac{\partial T}{\partial t} + \boldsymbol{u} \cdot \nabla T = \kappa \nabla^2 T + H, \tag{3}$$

where $\boldsymbol{u}$ is the velocity vector, $\boldsymbol{\tau}$ is the deviatoric stress tensor, p is the pressure, ρ is the density, $\boldsymbol{g}$ is the gravitational acceleration, T is the temperature, t is the time, κ is the thermal diffusivity, and H is the temperature source term accounting for both internal heating and the latent heat of fusion.

To alleviate computational costs associated with simulating plume-lithosphere interaction in 3-D, we simulate only one quarter of the rising plume under the assumption of rotational symmetry (Figure 2). We explore a range of lithospheric thicknesses and set the initial temperature condition using an error function according to

$$T(z) = \begin{cases} T_{surf} + (T_m - T_{surf})\ \mathrm{erf}\left(\dfrac{h - z}{2\sqrt{\kappa t_{lt}}}\right) & \text{if } z > z_0 \\ T_{CMB} - (T_{CMB} - T_m)\ \mathrm{erf}\left(\dfrac{z}{2\sqrt{\kappa t_a}}\right) & \text{if } z \le z_0 \end{cases} \tag{4}$$

where T_{surf} is the surface temperature, T_{CMB} is the CMB temperature, T_m is the ambient mantle temperature, z is the height above the CMB, z_0 is the height of the entire lower mantle, h is the thickness of the whole mantle, and t_{lt} and t_a are artificial ages that are constant across all cases and are used to setup the initial thermal boundary layers. Note that, unless explicitly otherwise mentioned, all temperatures referred to are potential temperatures. Away from the plume and thermal boundary layers, $T(z)$ remains nearly constant throughout the mantle (i.e., $T(z) \approx T_m$). We initiate a mantle plume at the CMB by perturbing the initial temperature within a radius of 200 km (d_0) from the plume center (Figure 2a) according to

$$T(z) = T_{CMB} - (T_{CMB} - T_m)\ \mathrm{erf}\left(\frac{z}{2\sqrt{C\kappa t_a}}\right) \text{ if } z \le z_0 \text{ and } d < d_0, \tag{5}$$

where $d = \sqrt{x^2 + y^2}$ is the horizontal distance to the axis of rotational symmetry and

$$C = \left(-5 \times 10^{-11}\right) d^2 + 3. \tag{6}$$

Mechanical boundary conditions at the upper, lower, and symmetric boundary planes (i.e., on $x = 0$ and $y = 0$) prevent normal flow, and no vertical flow (i.e., $v_z = 0$) is imposed on the remaining two vertical sides. Temperature boundary conditions are set to 273 K at the surface of the domain and either 1873, 1973, 2073, or 2173 K at the domain's base, with the latter controlling the resulting plume excess temperature (which is inherently smaller than the excess temperature at the CMB). All other boundaries are treated as insulating (i.e., $\frac{\partial T}{\partial \mathbf{n}} = 0$, where $\mathbf{n}$ is the normal vector).

Our simulations contain two distinct materials that are tracked by material volume fraction fields (e.g., Garel et al., 2014; Wilson, 2009)—a 10 km-thick crustal layer of reference density 2,900 kg m^{-3} and an underlying mantle of reference density 3,300 kg m^{-3}. Three deformation mechanisms are generally considered: (a) plastic deformation (defined using the Byerlee yield-stress law for brittle materials); (b) diffusion creep; and (c) dislocation creep. For each mechanism, the corresponding viscosity is calculated according to

$$\mu_{plas} = \frac{\min\left\{C_c + f_c P, \tau_{max}\right\}}{2\dot{\epsilon}}, \tag{7}$$

$$\mu_{diff} = A_{diff}^{-1} \exp\left(\frac{E_{diff} + PV_{diff}}{RT_a}\right), \tag{8}$$

$$\mu_{disl} = A_{disl}^{-\frac{1}{n}} \dot{\epsilon}^{\frac{1-n}{n}} \exp\left(\frac{E_{disl} + PV_{disl}}{nRT_a}\right), \tag{9}$$

where C_c is the surface yield strength, f_c is the friction coefficient, P is the lithostatic pressure, τ_{max} is the maximum yield strength, $\dot{\epsilon}$ is the second invariant of the strain-rate tensor, A is the viscous creep prefactor, E is the activation energy controlling the temperature-dependence of viscosity, V is the activation volume controlling its pressure dependence, R is the molar gas constant, T_a is the temperature (which includes the effect of adiabatic compression), and n is the stress exponent in the dislocation creep regime. For diffusion creep, it has long been recognized that there is a viscosity increase between the upper and lower mantle (e.g., Hager et al., 1985), and we therefore include a viscosity transition in the depth range of 660 $\pm$ 60 km. Over that region, A_{diff}, E_{diff}, and V_{diff} vary from upper- to lower-mantle values (e.g., Nakada et al., 2018) according to

$$A_{diff}^{trans} = \exp\left(\frac{\ln A_{diff}^{UM} + \ln A_{diff}^{LM}}{2} + \frac{\ln A_{diff}^{UM} - \ln A_{diff}^{LM}}{2} \tanh\frac{z - z_0}{\sigma}\right), \tag{10}$$

$$E_{diff}^{trans} = \frac{E_{diff}^{UM} + E_{diff}^{LM}}{2} + \frac{E_{diff}^{UM} - E_{diff}^{LM}}{2} \tanh\frac{z - z_0}{\sigma}, \tag{11}$$

$$V_{diff}^{trans} = \frac{V_{diff}^{UM} + V_{diff}^{LM}}{2} + \frac{V_{diff}^{UM} - V_{diff}^{LM}}{2} \tanh\frac{z - z_0}{\sigma}, \tag{12}$$

where superscripts UM and LM denote, respectively, upper-mantle and lower-mantle parameters, and σ is a depth-scaling factor (set to 20 km). The effective viscosity, μ, of the full material is given by

$$\mu = \left(\frac{1}{\mu_{\text{plas}}} + \frac{1}{\mu_{\text{disl}}} + \frac{1}{\mu_{\text{diff}}} \right)^{-1} \tag{13}$$

and is shown in Figure 2b. It is important to note that only plastic deformation is permitted within the crust (i.e., dislocation and diffusion creep are neglected). The average viscosity at the interface between crust and mantle is calculated through a geometric mean of the overlying and underlying effective viscosities. In the upper mantle, using the physical constants listed in Table 1, we find that dislocation creep is mostly restricted to within the plume, where temperatures and stresses are highest. Dislocation creep does not manifest in the lower mantle.

Under the specified initial conditions, boundary conditions, and choice of material properties (Table 1), plumes generally require ~100 Myr to develop and ascend through the mantle, from the CMB to the uppermost mantle. During this period, the lithosphere undergoes significant cooling and thickening due to surface-driven conductive heat loss. To enable analysis of plume-lithosphere interactions at lithospheric thicknesses representative of modern oceanic basins, we reset the thermal structure of the upper mantle above ~300 km when the plume head is about to reach this depth (Figure 2c). Specifically, we replace t_{lt} with a representative initial lithospheric age t_{i} in Equation 4. In our simulations, we define the base of the lithosphere as the 1448 K (i.e., 1175°C) temperature isosurface, adjusted for adiabatic compression using a temperature gradient of 0.4 K · km^{-1}.

2.2. Tracking Partial Melting

To quantify partial melting and track associated changes in melt composition through space and time, we couple the BDD21 peridotite melting and melt chemistry framework (Ball et al., 2022; Duvernay et al., 2024) to Lagrangian particle advection within Fluidity (Mathews, 2021). Starting at the point when upper-mantle temperatures are reset, particles are initialized within the plume in the upper mantle (Figure 2c). In each particle, melt and residual solid form a closed system, such that melt is not extracted (i.e., we do not model two-phase flow). They are advected upwards via mantle flow and new particles are continually initialized as more plume material enters the upper mantle. At each time step, particles query their interpolated coordinates and temperature from the underlying finite element mesh, update the temperature to account for adiabatic compression, and pass these values to BDD21. These parameters are used in BDD21 to estimate peridotite mineralogy, partial melting, element partition coefficients, and trace element concentrations in both the generated magma and residual peridotite. Each particle tracks the evolution of its corresponding mineralogy, melting, and instantaneous melt chemistry, such that its past history is used to inform subsequent predictions.

Partial melting commences once a particle crosses the solidus and continues as long as the calculated degree of melting, F, surpasses the highest degree of melting previously recorded by this particle, F_{max}. The instantaneous melting rate, M, is calculated by dividing the increment in F by the time step, Δt, such that

$$M = \max\left(\frac{F - F_{\text{max}}}{\Delta t}, 0 \right). \tag{14}$$

The only feedback of melting on simulation dynamics is through absorption of latent heat (i.e., melting does not affect the buoyancy or viscosity of solid material). Absorption of latent heat is modeled using thermodynamic considerations developed by McKenzie (1984) and modified by Duvernay et al. (2021) to account for deviations from adiabatic processes—the resulting decrease in temperature is fed back to the finite element nodes as a source term in the energy equation. Composition- and porosity-induced melt buoyancy and melt re-freezing are neglected. Knowing F and M, residual solid and instantaneous melt compositions for each particle are updated according to the fractional melting formulation of R. S. White et al. (1992), which leverages previous works on element partitioning (e.g., Shaw, 1979; C. Sun & Liang, 2013; Wood & Blundy, 2014). All liquid concentrations remain null in the absence of melting and, if a given element is exhausted in the residual solid, its instantaneous liquid concentration is set to zero. For all simulations examined herein, we assume a constant water content of 200 ppm in the source, in line with estimates for typical plumes beneath oceanic lithosphere (e.g., Asimow & Langmuir, 2003; Wallace, 1998). While we acknowledge that water concentrations vary in the mantle (e.g.,

Table 1
Physical Parameters Used in Geodynamical Simulations and Definitions of Plume-Related Diagnostics

Parameter	Symbol	Value	Units
Crust reference density	ρ_c	2.9×10^{3}	$kg\cdot m^{-3}$
Mantle reference density	ρ_m	3.3×10^{3}	$kg\cdot m^{-3}$
Gravitational acceleration	g	9.81	$m\cdot s^{-2}$
Thermal expansion coefficient	α	3×10^{-5}	K^{-1}
Molar gas constant	R	8.3145	$J\cdot K^{-1}mol^{-1}$
Thermal diffusivity	κ	1×10^{-6}	$m^2\cdot s^{-1}$
Entropy of fusion	ΔS	407	$J\cdot kg^{-1}K^{-1}$
Lower-mantle thickness	z_0	2230	km
Whole mantle thickness	h_{CMB}	2890	km
Ambient mantle temperature	T_m	1573	K
Surface temperature	T_{surf}	273	K
Core-mantle boundary temperature	T_{CMB}		K
Excess temperature at CMB	ΔT_{CMB}		K
Artificial initial lithospheric age	t_{lt}	10	Myr
Artificial initial age at CMB	t_a	100	Myr
Radioactive temperature source	H_r	4×10^{-15}	$K\cdot s^{-1}$
Upper-mantle adiabatic gradient	ϕ_{UM}	0.4	$K\cdot km^{-1}$
Lower-mantle adiabatic gradient	ϕ_{LM}	0.3	$K\cdot km^{-1}$
Maximum viscosity	μ_{max}	5×10^{23}	$Pa\cdot s$
Minimum viscosity	μ_{min}	1×10^{18}	$Pa\cdot s$
Depth-scale factor	σ	20	km
Plastic deformation			
Crust surface yield strength	C_c	1×10^{8}	Pa
Crust friction coefficient	f_c	5×10^{-1}	–
Maximum yield strength	τ_{max}	1×10^{10}	Pa
Mantle surface yield strength	C_m	2×10^{6}	Pa
Mantle friction coefficient	f_m	2×10^{-1}	–
Upper-mantle diffusion creep			
Activation energy	E_{diff}^{UM}	268	$kJ\cdot mol^{-1}$
Activation volume	V_{diff}^{UM}	3.8×10^{-6}	$m^3\cdot mol^{-1}$
Prefactor	A_{diff}^{UM}	3.1×10^{-11}	$Pa^{-1}\cdot s^{-1}$
Lower-mantle diffusion creep			
Activation energy	E_{diff}^{LM}	180	$kJ\cdot mol^{-1}$
Activation volume	V_{diff}^{LM}	1.4×10^{-6}	$m^3\cdot mol^{-1}$
Prefactor	A_{diff}^{LM}	1.5×10^{-16}	$Pa^{-1}\cdot s^{-1}$
Mantle dislocation creep			
Activation energy	E_{disl}	530	$kJ\cdot mol^{-1}$
Activation volume	V_{disl}	1.4×10^{-5}	$m^3\cdot mol^{-1}$
Prefactor	A_{disl}	5×10^{-16}	$Pa^{-n}\cdot s^{-1}$
Exponent	n	3.5	–
Plume diagnostics		Eq. no.	
Buoyancy flux	Q_b	Equation 15	$Mg\cdot s^{-1}$
Volumetric melt production rate	V_m	Equation 16	$km^3\cdot Myr^{-1}$

Table 1
Continued

Parameter	Symbol	Value	Units
Average temperature of melts	$\overline{T}_{\mathrm{melt}}$	Equation 17	K
Average excess temperature of melts	$\Delta\overline{T}_{\mathrm{melt}}$	Equation 18	K
Average degree of melting	$\overline{F}$	Equation 19	–
Average concentration of trace element in melt	$\overline{c}_l$	Equation 20	ppm
Initial lithospheric age at re-initialization	t_{i}		Myr
Initial lithospheric thickness	h_{i}		km
Lithospheric thickness above conduit	h_{c}	Equation 21	km
Reference lithospheric thickness	h_{r}	Equation 21	km
Lithospheric thickness difference	Δh	Equation 21	km

Bolfan-Casanova, 2005), water only affects melt generation in our simulations and varying it from 0 to 200 ppm does not significantly alter the geochemical trends presented.

2.3. Plume-Related Diagnostics

To quantify plume vigor, as a post-processing step, we compute the buoyancy flux, Q_{b}, at each timestep using

$$Q_{\mathrm{b}} = 4\iint_{D} u_z \alpha \Delta T \rho_{\mathrm{m}}\ \mathrm{dS}, \tag{15}$$

where u_z is the vertical velocity, α is the thermal expansion coefficient, ΔT is the excess temperature, and D is the plume cross-sectional area within a horizontal plane at 660 km depth, which we demarcate based on where excess temperatures are at least 50 K above ambient mantle at that depth. The leading factor of four accounts for the fact that we are only simulating one quarter of the plume. We note that Q_{b} in Equation 15 represents a mass flux, although we retain the "buoyancy flux" terminology for consistency with existing literature. In addition, the volumetric melt production rate, V_{m}, at each timestep is calculated using

$$V_{\mathrm{m}} = 4\iiint_{\Omega} M\ \mathrm{dV}, \tag{16}$$

where Ω represents the integration domain. The average temperature of all melts produced at a given timestep, $\overline{T}_{\mathrm{melt}}$, is obtained by integrating the corresponding temperature (excluding the effects of adiabatic decompression) on particles, weighted by their individual melting rates

$$\overline{T}_{\mathrm{melt}} = \frac{4\iiint_{\Omega} TM\ \mathrm{dV}}{V_{\mathrm{m}}}. \tag{17}$$

The average excess temperature is therefore defined as

$$\Delta\overline{T}_{\mathrm{melt}} = \overline{T}_{\mathrm{melt}} - T_{\mathrm{m}}. \tag{18}$$

In a similar manner, the average degree of melting, $\overline{F}$, is calculated using

$$\overline{F} = \frac{4\iiint_{\Omega} FM\ \mathrm{dV}}{V_{\mathrm{m}}}, \tag{19}$$

and the average concentration of each trace element in the primary melt, $\overline{c}_l$, is calculated using

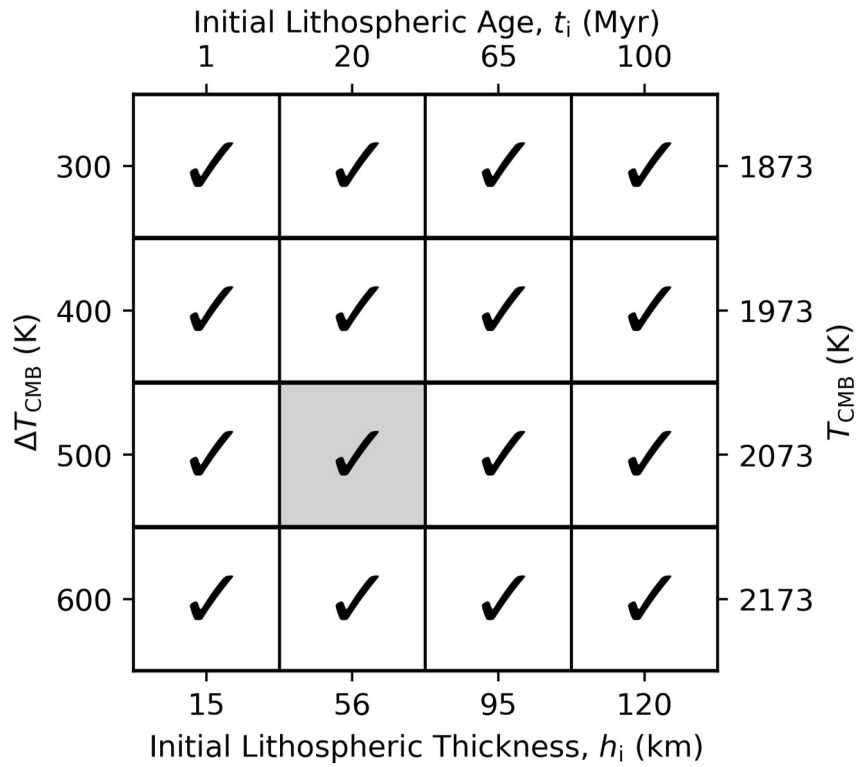

Figure 3. Cases examined, defined by their respective values of plume excess temperature at the core-mantle boundary (CMB), ΔT_{CMB}, and initial lithospheric thickness, h_i. Corresponding CMB temperatures (T_{CMB}) and equivalent initial oceanic lithospheric ages (t_i) are also indicated. The reference case ΔT500_LT56 is highlighted in gray.

$$\overline{c}_l = \frac{4\iiint_\Omega c_l M \, \mathrm{dV}}{V_m}. \tag{20}$$

Since these diagnostics are weighted by M, they incorporate a greater contribution from regions with higher melting rates, which are anticipated to dominate the signature of erupted lavas. Note that, in all equations and unless otherwise specified, Ω encompasses the entire melting region (i.e., where $M > 0$). When obtaining average trace-element concentrations, however, we have also considered the following two additional strategies to define Ω: (a) integrate only those particles that generate melts within a 50 km or 100 km radius from the plume axis; and (b) integrate only those particles generating melts within a distance d_{max} of the plume axis that is delimited by the furthest away particle with a maximum melting-rate of either 0.1 or 0.05 Myr^{-1}. For the latter strategy, d_{max} varies from case to case and, for some cases, is zero due to insufficient melting (see Table S1 in Supporting Information S1). Such selection strategies are motivated by two-phase flow models of mid-ocean ridge dynamics that suggest melts are only focused into the ridge axis if they are generated within a horizontal distance of ~60 km of the spreading center (e.g., Keller et al., 2017; Sim et al., 2020). We consider it important to determine the sensitivity of our melt-related diagnostics to these choices, but the simulation outcomes turn out to be insensitive to imposing these melt-focusing restrictions—a result that is consistent with the fact that the majority of plume melting occurs within the core of the conduit.

2.4. Individual Cases Examined

We begin by examining a reference simulation labeled ΔT500_LT56, where the naming convention denotes $\Delta T_{CMB} = 500$ K and the initial lithospheric thickness, $h_i = 56$ km. To investigate the sensitivity of results to both plume excess temperature and lithospheric thickness, we analyze an additional 15 cases, systematically varying ΔT_{CMB} from 300 to 600 K in increments of 100 K, and h_i from 15 to 120 km in increments of ~30–40 km. A summary of all cases is provided in Figure 3.

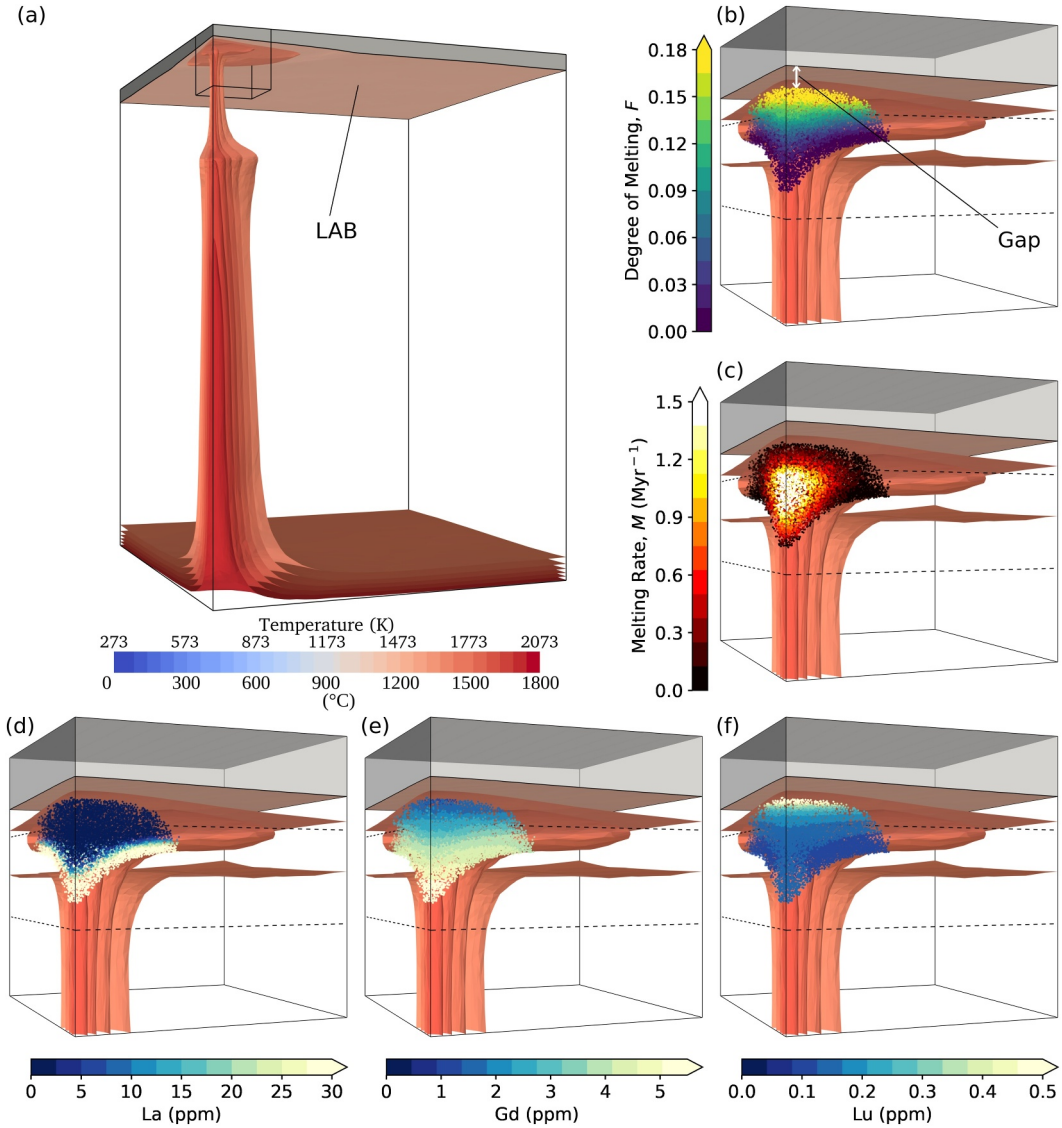

Figure 4. Snapshots of the plume geometry and melting characteristics for the reference case, ΔT500_LT56, at $t = 8$ Myr (i.e., 8 Myr after the lithospheric structure was reinitialized). (a) Temperature isosurfaces of the plume, ranging from 1673 to 1973 K at intervals of 60 K. The lithosphere is shown as a gray block, and the lithosphere-asthenosphere boundary (LAB) is represented by the first underlying isosurface (1448 K). The small black cube with 300 km sides delimits the plume-head region illustrated in all other panels. (b) Blow up of the plume melting region with isosurfaces overlain by particles colored by the degree of melting, F. Only particles with melting rate $M > 0$ are shown, illustrating that the top of the melting region does not fully extend to the LAB, but is separated by a prominent gap. Dashed horizontal lines mark depths of 100 and 200 km beneath the surface. (c) Same except particles are colored by melting rate, M. (d–f) Same except particles are colored by instantaneous liquid concentrations of La, Gd, and Lu (i.e., a representative light, middle, and heavy rare earth element, respectively).

3. Results

3.1. Reference Case

We begin by describing the spatio-temporal evolution of the flow regime, thermal structure, and melting diagnostics for the ΔT500_LT56 reference simulation (Figure 4). Shortly after model initiation, a plume head forms above the thermal boundary layer and ascends through the mantle, underlain by a trailing feeder conduit (Figures S1a–S1e in Supporting Information S1). As the plume head rises, its width increases during lower-mantle ascent,

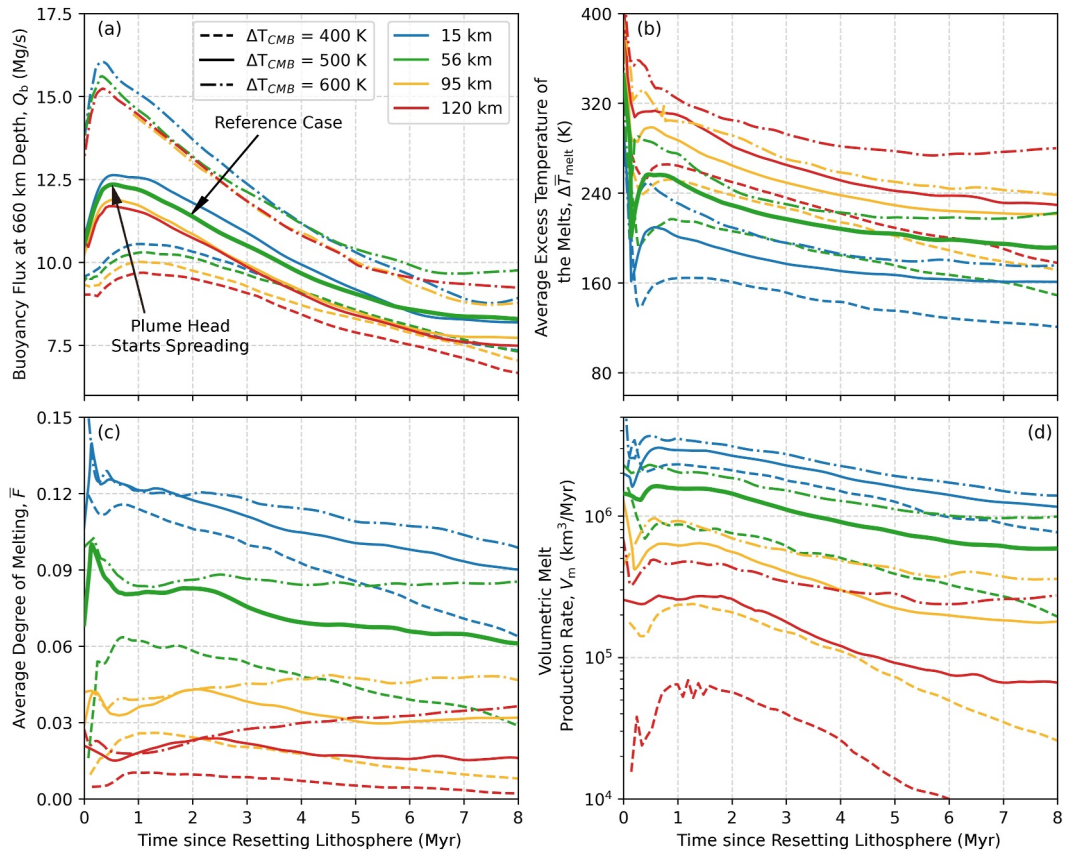

Figure 5. Temporal variation of selected model diagnostics for simulations across a range of plume excess temperatures, ΔT_{CMB}, and initial lithospheric thicknesses. Bold line = reference case, ΔT500_LT56. (a) Buoyancy flux, Q_b, at the lower-to-upper mantle boundary (660 km depth). (b) Average excess temperature of melts, $\Delta\overline{T}_{melt}$, within the melting region. (c) Same for average degree of melting, $\overline{F}$. (d) Volumetric melt production rate, V_m, across the full melting region.

before narrowing significantly upon entering the lower-viscosity upper mantle (Figures S1f–S1h in Supporting Information S1). In the upper mantle, the plume ascends rapidly and, upon interaction with the lithosphere, spreads radially beneath the LAB (Figure 4a). Over time, this spreading forms a low-viscosity asthenospheric channel, fed by rapidly ascending material from the plume tail, which continues to narrow within the upper mantle. Eventually, the system evolves to a stage where melting is confined to the center of the plume tail (Figure S2 in Supporting Information S1). It is at this point that we focus our analyses.

To identify an appropriate simulation time for investigating and comparing melt diagnostics across models, we analyze temporal changes in plume characteristics during the first 8 Myr following the resetting of the lithospheric thermal structure (green bold solid line in Figure 5). This resetting typically precedes the onset of magma production by 0.02–0.15 Myr. For the reference case, the buoyancy flux, Q_b, initially increases rapidly until 0.5 Myr as the plume head arrives, then gradually declines asymptotically until ~6 Myr as the plume head spreads out and wanes, with the maximum Q_b roughly corresponding to the start of plume-head spreading (Figure 5a). Simulated values of Q_b are generally higher than observational estimates (Hoggard, Parnell-Turner, & White, 2020; King & Adam, 2014; Sleep, 1990), which we discuss in Section 4.5. The average excess temperature of melts, $\Delta\overline{T}_{melt}$, initially drops rapidly because initial melts are all generated close to the solidus where temperatures are high, but as melting progresses, more melts from shallower, cooler regions start to contribute (Figure 5b). $\Delta\overline{T}_{melt}$ subsequently rebounds as the plume head continues to spread out and wane and the contribution of low-degree, low-temperature melt pockets near the edges of the plume head drops. After 2 Myr, these melt pockets vanish and the melting region becomes predominantly fed by ascending plume-tail material. This transition stabilizes the melting region, as indicated by the steady behavior of $\Delta\overline{T}_{melt}$ and average degree of melting ($\overline{F}$, Figures 5b and 5c).

Weighting by the melting rate (M) emphasizes high-productivity regions at the conduit center while minimizing the influence of lower-productivity melt pockets within the spreading plume-head, aligning more closely with the volumetric distribution of erupted basalts. Following establishment of the melting region, $\overline{F}$ increases initially, then tracks $\Delta\overline{T}_{\mathrm{melt}}$ from ∼2 Myr onwards, approaching a quasi-steady state as temperatures stabilize. However, an absolute steady state is never reached due to conductive lithospheric thickening and transient instabilities in the lower thermal boundary layer. Consistent with these trends, the volumetric melt production rate first rises and then falls as melting transitions from the plume head to the plume tail before stabilizing (Figure 5d). In the reference case, melt production reaches a peak of 2×10^6 km^3 Myr^{-1} in the plume head and stabilizes within a range of $0.5–1.0 \times 10^6$ km^3 Myr^{-1} in the plume tail.

These results indicate that ∼8 Myr after resetting of the lithospheric temperature structure is an optimal and appropriate time-frame for investigating the causes of observed trends in OIB chemistry. This choice of timing is supported by the following: (a) plume-head melting has waned—by this point, melting associated with the plume-head has diminished, and all melts are generated within the plume tail (Figure 5 and Figure S2 in Supporting Information S1); (b) stabilization of key features—plume temperatures beneath the lithosphere, the shape of the melt region, and melt diagnostics have reached a relatively stable state (Figure 5); and (c) avoidance of further lithospheric thickening—beyond this time, conductive thickening of the lithosphere reduces the range of lithospheric thicknesses available for analysis, limiting the scope of the investigation. For the remainder of this study, unless otherwise stated, simulation times are reported relative to the resetting of the lithospheric thermal structure and model diagnostics are evaluated at 8 Myr.

Figure 4 provides a snapshot at $t = 8$ Myr, illustrating the degree of melting, melting rate, and selected REE concentration of instantaneous melts across the model domain. Complementary 3-D views of mineral modal abundances in the residue are shown in Figure S3 in Supporting Information S1. In Figure 6, these quantities are averaged as a function of depth within a 20 km-radius quarter-cylinder centered on the plume axis.

The melting region is thinnest at its base, where melting is confined to the hotter central core of the conduit. As plume material rises and pressure decreases, melting occurs at lower temperatures, causing the melt region to expand horizontally and adopt an inverted conical shape (Figure 4b). The melting rate M is highest at the center of the plume and decreases radially toward the margins (Figure 4c), reflecting variations in the rate of change in F along flow trajectories, which are governed by regional temperature and pressure gradients.

Notably, the melting region does not extend to the base of the lithosphere, leaving a prominent gap between the top of the melting region and the LAB (Figures 4b and 4c). This gap indicates a negative F gradient along the flow trajectories in this zone, preventing the generation of new melts (Figure S4 in Supporting Information S1). The negative gradient arises from a significant temperature drop near the LAB, where heat transfer transitions from convective to conductive. This temperature decrease counteracts and surpasses the decompression effect that typically facilitates melting, effectively limiting melt production in this region.

Instantaneous REE concentrations in melts (i.e., concentrations produced at a specific time) are strongly influenced by the degree of melting (F) and the garnet-to-spinel transition. La, as a highly incompatible LREE, reaches peak concentration in the melt just above the solidus and is rapidly exhausted as melting progresses (Figures 4d and 6c). Similarly, Gd, a middle rare earth element shows a decrease in melt concentration with increasing F, although more gradually than La due to its lower incompatability (Figures 4e and 6d).

In contrast, Lu (a HREE) exhibits a distinct behavior. In the reference simulation, melting begins in the garnet stability field and ends in the garnet-to-spinel transition zone, where both spinel and garnet are present in the residue. Because Lu is compatible in garnet, its initial concentration in the melt remains relatively low and stable. As pressure decreases, garnet is progressively replaced by orthopyroxene, reducing the bulk partition coefficient of Lu in the residual peridotite. This shift forces more Lu into the melt, causing a steady increase in its concentration (Figure 6 and Figure S3 in Supporting Information S1). A pronounced rise in Lu concentration occurs as garnet approaches exhaustion (Figures 4f and 6e). During this process, clinopyroxene melts progressively (Figure 6h), and the modal abundance of olivine increases as melting intensifies (Figure 6f). Spinel begins to form at ∼90 km depth but remains a minor phase, achieving a maximum modal abundance of ∼1% and persisting as a minor component after melting ceases (Figure 6i).

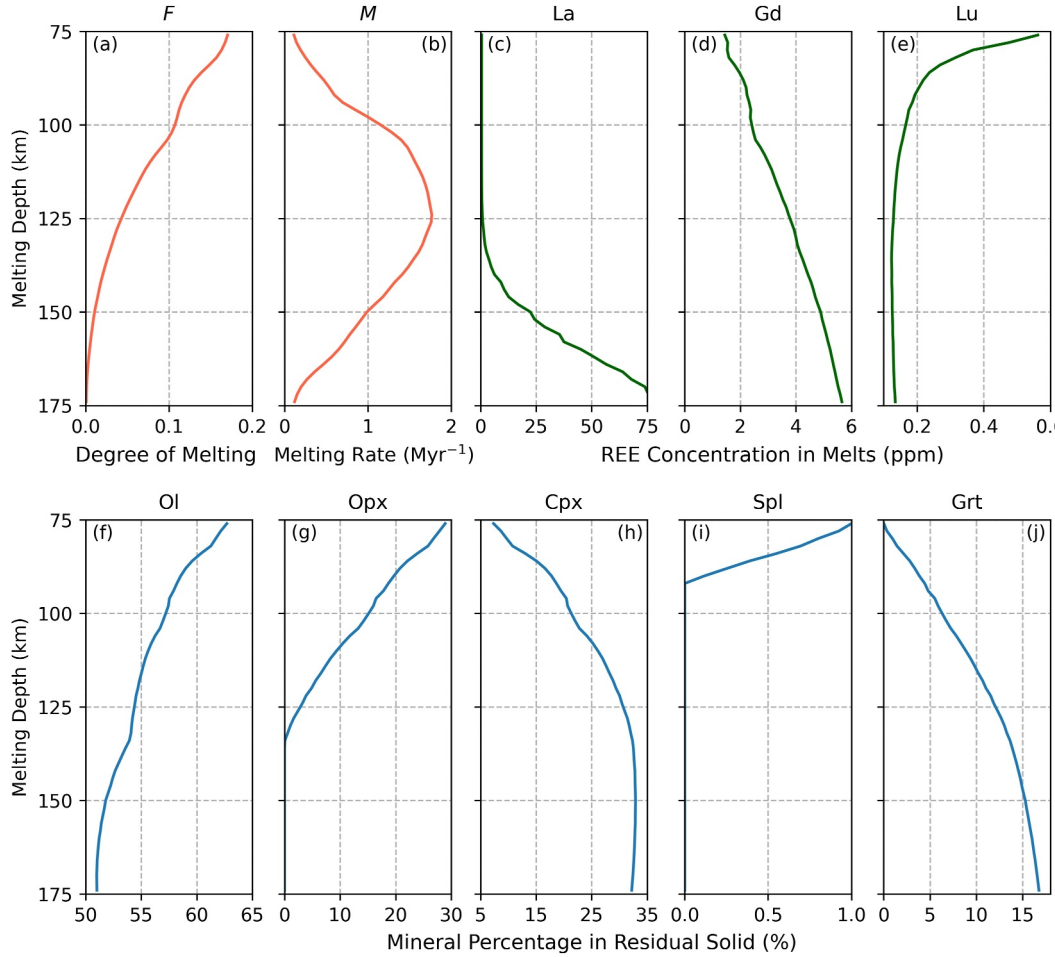

Figure 6. Depth-averaged melting and compositional parameters for the ΔT500_LT56 reference simulation at $t = 8$ Myr. (a) Degree of melting, F, averaged over a 20 km-radius quarter-cylinder centered on the plume axis. (b) Same for melting rate, M. (c–e) Same for La, Gd, and Lu concentrations in melts. (f–j) Same for mineral modal abundances in the residual solid. Ol = olivine; Opx = orthopyroxene; Cpx = clinopyroxene; Spl = spinel; Grt = garnet.

3.2. Sensitivity of Melting to Excess Temperature and Lid Thickness

3.2.1. Melt Region Geometry, Degree of Melting, and Melting Rate

We now explore how model diagnostics vary with plume excess temperature and lid thickness. In general, melting-region diagnostics stabilize after ∼6 Myr, reaching quasi-steady-state values at 8 Myr. Their temporal evolution, shown in Figure 5, reflects the interplay between plume buoyancy flux and lithospheric thickening. The initial drop in $\Delta\overline{T}_{\mathrm{melt}}$ occurs across all cases at the onset of melting, with stabilization taking longer in cases with thinner lithosphere due to the higher rate of lithospheric thickening (Figure 5b). After the transition to plume tail melting, $\Delta\overline{T}_{\mathrm{melt}}$ continues to decrease for cases with lower excess temperatures and thicker lithosphere (e.g., cases ΔT400_LT95 and ΔT400_LT120), while higher excess temperatures generally yield more stable values. Trends for $\overline{F}$ closely follow those of $\Delta\overline{T}_{\mathrm{melt}}$ (Figure 5c). An exception occurs in the ΔT600_LT120 case, where $\overline{F}$ gradually increases due to significant lithospheric thinning induced by the plume. Melt production rates within the plume tail generally decline over time as the lithosphere thickens (Figure 5d), with this decrease being more pronounced in cases with lower ΔT_{CMB} and initially thicker lithosphere. In these scenarios, insufficient heat supply from the plume cannot offset conductive heat loss to the surface. Across all cases examined, volumetric melt production rates range from zero to just over 1 million km^3 Myr^{-1}.

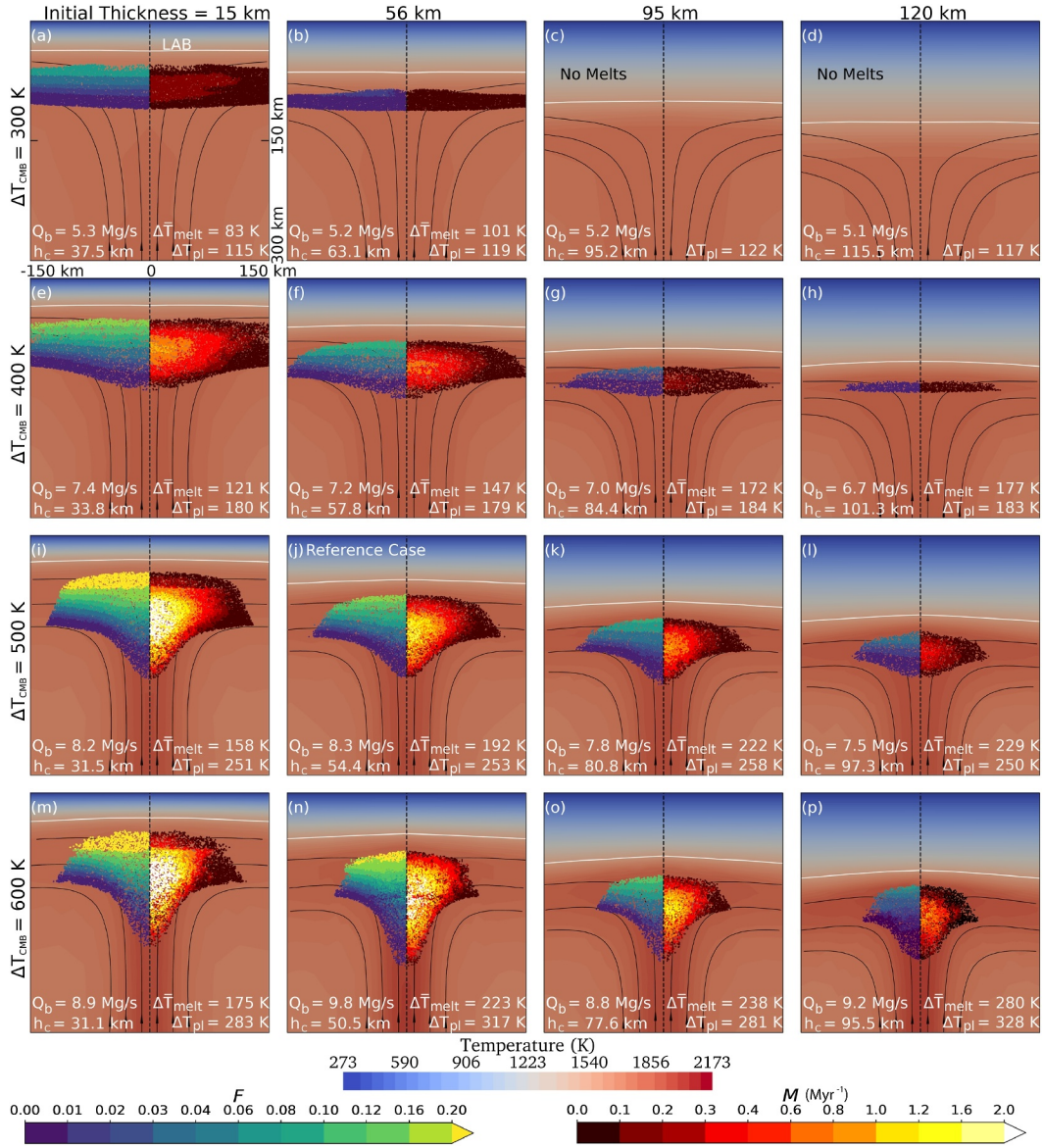

Figure 7. The degree of melting (F, left) and melting rate (M, right) in the melting region, at 8 Myr after the resetting of the lithospheric thermal structure, for plumes with different excess temperatures and initial lithospheric thicknesses. Initial lithospheric thicknesses (h_i) are labeled above each column, and ΔT_{CMB} is labeled to the left of each row. Buoyancy flux (Q_b) and lithospheric thickness above the plume center (h_c) is shown in the lower-left corner of each panel. Each plume's highest excess temperature before melting (ΔT_{pl}) and the average excess temperature of all melts ($\Delta \overline{T}_{melt}$) are labeled in the lower-right corner of each panel. The white line delineates the lithosphere-asthenosphere boundary, approximated via the 1448 K (1175°C) isotherm (adiabatic compression included; F. D. Richards, Hoggard, Crosby, et al., 2020). Our reference case ΔT500_LT56 is shown in panel (j), while other cases are shown in panels (a–i) and (k–p). Note that, in order to better highlight variations in F and M, the color bars have corresponding values that do not linearly increase.

To further illustrate the sensitivity of melt region geometry and variations in F and M to plume excess temperature and lid thickness, we present cross-sections for all 16 cases in Figure 7. Note that the lithospheric thickness above the plume center, h_c (indicated in the lower-left corner of each panel and delineated by white lines), differs from its initial value h_i due to time-dependent conductive heat loss and plume-lithosphere interactions.

At the reference lithospheric thickness (i.e., h_i =56 km), increasing ΔT_{CMB} leads to a deeper onset of melting, particularly in the hotter central core of the plume, while narrowing the melting region. This results in a transition from a disk-like to an inverted conical geometry, accompanied by an increase in both F and M (second column in

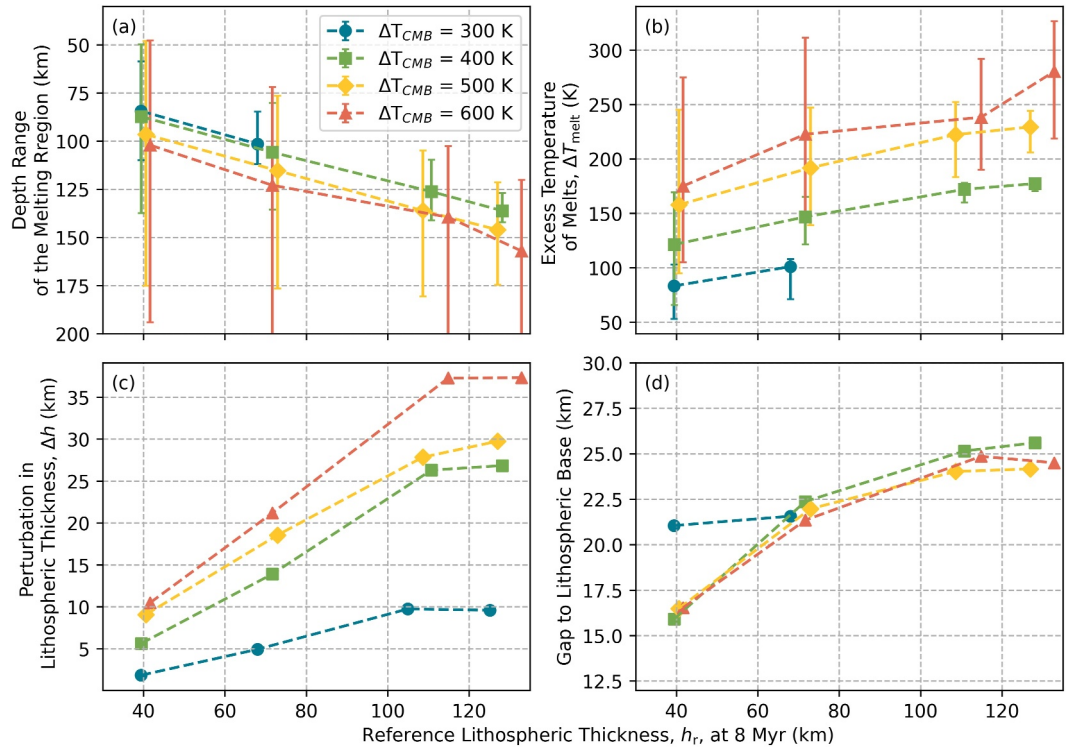

Figure 8. Characteristic melt diagnostics at 8 Myr after resetting the lithospheric thermal structure as a function of plume excess temperature and overlying lithospheric thickness. (a) Depth range of the melting region as a function of reference lithospheric thickness, h_r. Symbol = mean melting depth, weighted by M; error bars = maximum and minimum depths of melting. (b) Same for the average, minimum, and maximum excess temperature of melts, $\Delta\overline{T}_{melt}$. (c) Same for the perturbation in lithospheric thickness, Δh. (d) Same for the size of the gap between the top of the melting region and base of the lithosphere.

Figure 7). At the reference excess temperature (i.e., $\Delta T_{CMB} = 500$ K), increasing lithospheric thickness restricts the shallowest depth of plume melting but has minimal impact on the deepest melting depth, as the solidus remains below even the thickest lithosphere examined (third row in Figure 7 and yellow diamonds in Figure 8a). With increasing lithospheric thicknesses, the melting region flattens, resulting in an overall decrease in both F and M. Across all cases, the highest F occurs at the lowest pressure while M peaks at the central core of the plume.

In addition to these general observations, several notable trends in melting diagnostics are evident across the examined parameter space:

1. When ΔT_{CMB} is limited to 300 K, corresponding to $\Delta T_{pl} \leq 130$ K, melting occurs only beneath lithosphere thinner than ~75 km.
2. Substantial melting beneath lithosphere thicker than 100 km is possible only when $\Delta T_{CMB} \geq 500$ K, corresponding to $\Delta T_{pl} \geq 250$ K.
3. At a given T_{CMB}, the maximum melting depth remains constant regardless of lithospheric thickness, causing the average melting depth (weighted by melting rate) to increase more slowly than the corresponding reference lithospheric thickness (Figure 8a).
4. The average excess temperature of melts $\left(\Delta\overline{T}_{melt}\right)$ represents only 30%–70% (Figure 7) of the imposed CMB excess temperature $\left(\Delta T_{CMB}\right)$. This reduction occurs because the plume cools during ascent and latent heat is absorbed during melting. For plumes with the same h_i, the increase in ΔT_{melt} is significantly smaller than the corresponding increase in ΔT_{CMB}.
5. $\Delta\overline{T}_{melt}$ increases with both ΔT_{CMB} and lithospheric thickness (Figures 7 and 8b). Higher ΔT_{CMB} leads to increased melt production, despite thermal rejuvenation of the lithosphere and latent heat absorption providing a modulating effect. Thicker lithosphere elevates $\Delta\overline{T}_{melt}$ by increasing the average melting pressure and reducing melt production rates.

6. At a given ΔT_{CMB}, the range of individual excess melt temperatures narrows as lithospheric thickness increases. Conversely, for a fixed lithospheric thickness, increasing ΔT_{CMB} broadens this range (Figure 8b).

3.2.2. Impact on Lithospheric Thickness

Plume-lithosphere interaction induces both spatial and temporal variations in lithospheric thickness. Thinning occurs through two main mechanisms: mechanical displacement, where the upwelling plume pushes aside lithospheric material, and thermal rejuvenation, where conductive heat transfer from the hot plume counteracts diffusive thickening. There is no net horizontal motion of the lithosphere with respect to the plume conduit in our simulations, resulting in the greatest thinning directly above the plume center (Figures 4a and 7) and the thickest lithosphere at the furthest distances from the plume.

To quantify the plume's impact on lithospheric thickness, we compare the thickness above the plume conduit, h_c, with a reference lithospheric thickness, h_r, defined as the average thickness within a region spanning (x, y) = (1,500 km, 1,500 km) to (2,000 km, 2,000 km), ensuring it is distal from both the plume and simulation boundaries. The metric, Δh, quantifies the deviation between the expected lithospheric evolution in the absence of a plume and the actual lithospheric thickness above the plume conduit. It is calculated as:

$$\Delta h = h_r - h_c. \tag{21}$$

For a fixed CMB temperature anomaly, ΔT_{CMB}, Δh increases with initial lithospheric thickness h_i (Figure 8c). Older, thicker lithosphere contains a more substantial low-viscosity region near its base, making it more susceptible to deflection and deformation by an upwelling plume. As seen from the streamlines in Figure 7, lithospheric thickness modifies the underlying flow field and associated melting trajectories, creating a larger gap between the top of the melting column and the LAB (Figure 8d). These effects counteract one another in determining the shallowest melting depths. For ΔT_{CMB} = 300 K, the two processes roughly balance, but for hotter plumes, lithospheric deflection dominates, reducing the rate at which shallow melting depths increase with lithospheric thickness. This suggests that plume-driven lithospheric modification can partially counteract the expected *lid effect* in thicker lithosphere.

For a fixed value of initial lithospheric thickness, increasing ΔT_{CMB} intensifies lithospheric thinning (Figure 8c). Hotter plume material more effectively transfers heat to the lithosphere and induces greater mechanical displacement due to increased buoyancy. As a result, lithospheric thickness above the plume center decreases with higher ΔT_{CMB}. However, the gap between the melting region and the overlying lithosphere remains largely unchanged by ΔT_{CMB} (Figure 8d). Across all cases, the largest lithospheric thickness perturbation of 36 km (~20%) is observed in the ΔT600_LT120 case.

3.3. Geochemical Trends

Having explored the sensitivity of melt-region characteristics across our parameter space, we now assess their impact on the predicted geochemical diagnostics of plume-derived melts and compare our numerical predictions with OIB observations. Figure 9 illustrates the La, Gd, and Lu concentrations, as well as λ_0, λ_1, and λ_2 values, for all instantaneous melts generated throughout the entire melting region, weighted by their melting rate M. Average trace element concentrations are presented with error bars indicating the 10th and 90th percentiles, as percentiles are more appropriate than standard deviations for these data that do not follow a Gaussian distribution. However, we do not evaluate the range of REE pattern shape coefficients (λ_i) in the same way, as these coefficients do not systematically correlate with melt composition. Specifically, averaging two groups of melts produces intermediate element concentrations, but does not necessarily yield intermediate λ values, especially for λ_1 and λ_2. This is because the λ_i coefficients capture specific aspects of the REE pattern shape that can be non-linear and independent of the averaging process. Additionally, we remind the reader that the observational dataset from Jiang et al. (2024) comprises carefully selected OIB samples that have been corrected for olivine fractional crystallization to a common MgO content of 16 wt.%. This adjustment approximates parental magma compositions in equilibrium with mantle peridotites, ensuring a valid comparison with our simulation results.

Before presenting the geochemical trends from our numerical simulations, we reiterate (see Section 2.2) that the results remain consistent regardless of whether low-degree melts generated far from the plume axis are included or excluded from the integration (Figures S5–S8 in Supporting Information S1). This robustness suggests that

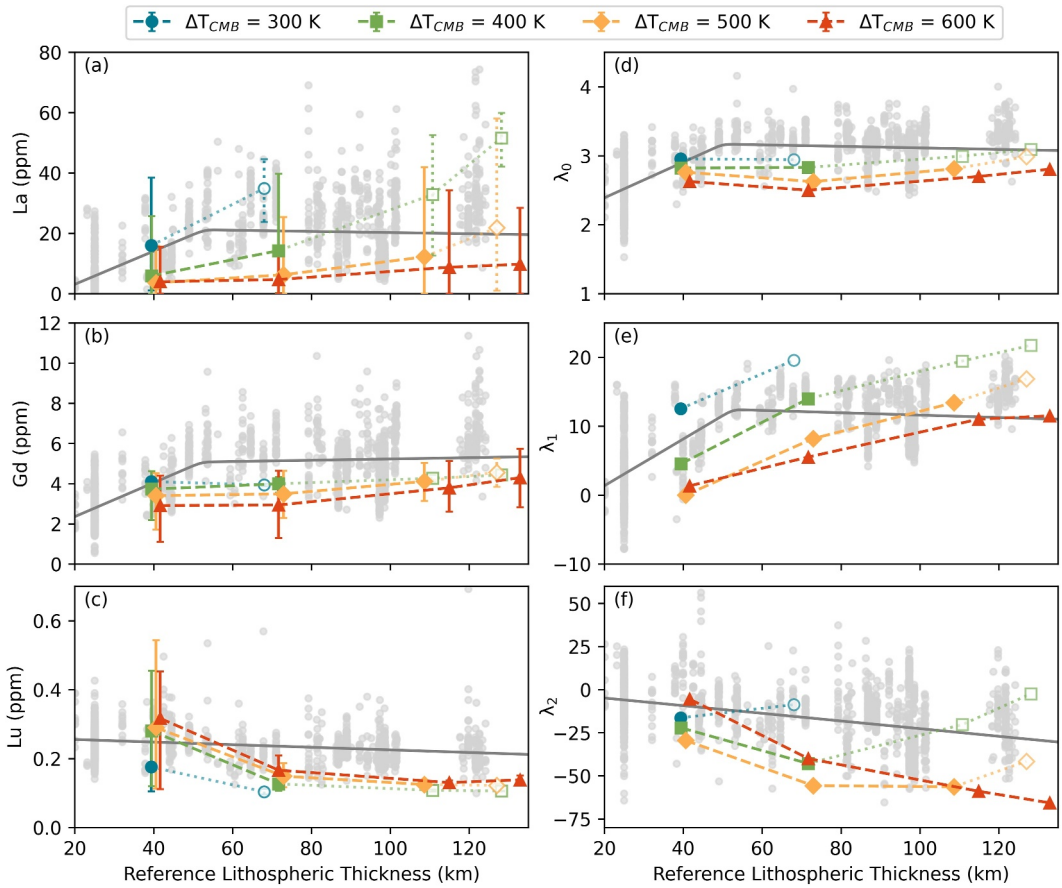

Figure 9. Compositional characteristics of instantaneous melts produced at 8 Myr after resetting the lithospheric thermal structure for plumes with a range of excess temperatures and overlying lithospheric thicknesses and a primitive mantle source. (a) Symbols = La concentrations (i.e., a light rare earth element). Averaged across the entire melting region, weighted by melting rate; error bars = 10th and 90th percentiles; open symbols = cases that have average degree of melting less than 2% (i.e., limiting their likelihood of being extracted to the surface and increasing their chance of being "filtered out", thereby illustrating the effect of a *melt-flux filter*); gray dots = composition of ocean island basalt samples corrected for effects of fractional crystallization back to a parental magma with MgO = 16 wt.% (Jiang et al., 2024); gray lines = best-fitting trends to these data using lithospheric thickness estimates derived from basin-specific plate-cooling models (Jiang et al., 2024). (b) Same for Gd (i.e., a middle rare earth element). (c) Same for Lu (i.e., a heavy rare earth element). (d–f) Same for λ_0, λ_1, and λ_2.

processes such as melt focusing or the incomplete extraction of small distal melt pockets have minimal influence on average melt compositions and their variability. Therefore, in the following sections, we focus on results obtained by integrating all melts across the melting domain.

3.3.1. Comparison With Observations

Overall, our simulations predict geochemical trends that align with many aspects of observed OIB data, though some notable exceptions arise.

LREEs: Highly incompatible elements, such as La, increase in concentration with thicker lithospheric lids due to lower melting degrees (F) and higher average melting pressures (Figures 9a and 10). This prediction range aligns with observations from our companion study, which show that La concentrations in OIBs rise with increasing lithospheric thickness up to ~55 km. However, beyond this threshold, observed values plateau, suggesting no further decrease in F (Jiang et al., 2024). In contrast, our simulations predict a continuous decrease in F with increasing lithospheric thickness, without stabilization (Figure 10). This discrepancy indicates that while the geodynamical models behave as expected theoretically, they do not fully capture observed trends. To reconcile this, Jiang et al. (2024) proposed the *melt-flux filter* hypothesis, where plumes with lower melt fluxes (e.g., those with lower excess temperatures) are not sampled in thicker lithosphere. Simulating this effect by excluding cases

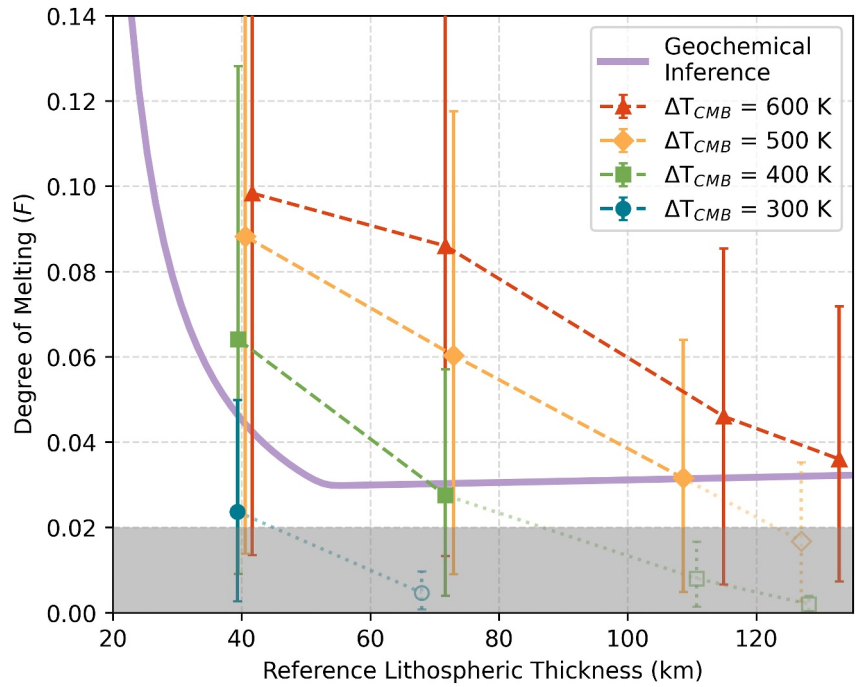

Figure 10. Average degree of melting across the entire melt region weighted by melting rate, $\overline{F}$, as a function of plume excess temperature and reference lithospheric thickness. Error bars = 10th and 90th percentiles; open symbols without face colors are as in Figure 9, showing cases that have average degree of melting less than 2%; gray shades = potential region where degree of melting is too low for extraction to surface, thereby illustrating the effect of *melt-flux filter*; purple line = average degree of melting F as a function of lithospheric thickness inferred from the bi-linear La concentration trend observed in global ocean island basalt samples (Jiang et al., 2024). This estimate is based on the La concentration ratio between the mantle source and the sample, assuming a fractional melting process.

with average melting degrees below 2%—a threshold for successful melt extraction—yields a close match to observed F trends (solid symbols in Figures 9a and 10). This hypothesis and its implications are further explored in Section 4.1.

MREEs: Moderately incompatible elements, such as Gd, show limited sensitivity to plume temperature and lithospheric thickness, remaining approximately constant across all cases, with minor dilution under thinner lithosphere (Figure 9b). However, this trend does not fully capture the observed bi-linear relationship described by Jiang et al. (2024), even when incorporating the *melt-flux filter*. Additionally, simulated Gd concentrations are systematically underestimated compared to observations.

HREEs: HREEs, such as Lu, behave differently due to their compatibility in garnet, which is stable at high pressure and low melting degrees. Simulated Lu concentrations decrease with increasing lithospheric thickness up to ~70 km, before stabilizing (Figure 9c). This two-domain behavior contrasts with the observed trend, where Lu concentrations decrease continuously, albeit with a very low gradient (Jiang et al., 2024). However, applying the *melt-flux filter* can generate a gradient similar to observations, though overall concentrations remain systematically underestimated.

REE pattern shape coefficients: Predictions for λ coefficients align reasonably well with observations when the *melt-flux filter* is applied (solid symbols in Figure 9d–9f). λ_0, the logarithmic mean REE concentration, remains nearly constant with increasing lithospheric thickness, consistent with the observed plateau above ~55 km. However, the increase in λ_0 at lower lithospheric thicknesses is not captured, as our simulation does not resolve melting beneath lithosphere thinner than ~40 km. Simulations also slightly underestimate observed λ_0 values. λ_1, which reflects LREE enrichment relative to HREEs, increases significantly with lithospheric thickness before stabilizing beyond a threshold, consistent with observations. λ_2, which represents the curvature of the REE pattern, steadily decreases, with the decrease-increase trend predicted in single-temperature cases disappearing

when the *melt-flux filter* is applied. While λ_2 is influenced by various factors, including melting degree and mineral assemblage, the overall trends are well captured, though absolute λ_2 values remain underestimated.

3.3.2. Melt Variability Across Melting Domain

In addition to average compositions, we also examine the range of elemental concentrations in instantaneous melts across the melting domain (error bars in Figures 9a–9c), revealing that: (a) La concentrations display broad variability across all combinations of plume temperature and lithospheric thickness; (b) Gd and Lu exhibit narrower ranges, though variability increases with plume temperature and is modulated by lithospheric thickness. In particular, Lu variability is enhanced beneath thinner lithosphere due to partitioning shifts near the garnet-spinel transition. These findings underscore the ability of a single plume to generate diverse melt compositions, especially under conditions of high plume temperatures and thin lithosphere. The implications of this variability for geochemical trends are further explored in Section 4.2.

4. Discussion

In this discussion, we systematically revisit each of the hypothesized behaviors introduced in Section 1, emphasizing key simulation results and performing additional tests where necessary to reinforce our interpretations.

4.1. Evidence for a Melt-Flux Filter

The *melt-flux filter* hypothesis, a generalization of the *temperature effect* hypothesis proposed by Jiang et al. (2024), implies a systematic bias whereby plumes with lower melt fluxes are progressively not sampled beneath thicker lithosphere. Our geodynamical simulations support this hypothesis, demonstrating that: (a) for lithosphere thinner than ∼55 km, plumes with a broad range of volumetric melt fluxes produce melts compatible with observations (Figure 10); (b) as lithosphere thickens beyond ∼55 km, plumes with lower melt flux are no longer reflected in the geochemical observations, likely because they generate insufficient melt volumes for extraction to the surface (Figures 7 and 10); and (c) older lithosphere experiences more efficient plume-driven thinning, meaning the actual lithospheric thickness above plumes is lower than predicted from seafloor age and theoretical plate-cooling models, with larger discrepancies for older seafloor. Our models highlight the key role of thermal rejuvenation in modulating oceanic lithospheric thickness and the depth-extent of plume melting (e.g., Li et al., 2004, Section 3.2.2).

Our simulations also allow us to assess the relative importance of plume excess temperature and lithospheric thinning. Results indicate that lithospheric thinning alone cannot explain the near-constant trend in observed F (∼3%; Figure 10) once the mechanical boundary layer thickness exceeds ∼55 km. Although our simulations show that plume-induced lithospheric thinning is more efficient in older lithosphere, minimum and average melting pressures still systematically increase with lithospheric thickness at constant excess temperature, albeit more gradually than expected from theoretical cooling models (Section 3.2.2). This discrepancy arises partly due to the gap between the LAB and the top of the melting region, which we identify here for the first time. This gap forms as plume material is redirected and cooled near the LAB, counteracting decompression and generating a negative F gradient that inhibits further melt production. Notably, the gap is more pronounced beneath older lithosphere (Figure 8d). Thus, while lithospheric thinning contributes to stabilizing the degree of melting, our results indicate that the primary control is the sampling of plumes with progressively higher melt fluxes. This behavior is essential for explaining observed OIB trace element trends, including the near-constant λ_1 trend beyond ∼55 km and the continuously decreasing λ_2 trend (Figures 9h and 9i). More effective lithospheric thinning under thicker lithosphere may provide an additional contribution to trends of highly incompatible elements and the associated degree of melting.

Our results suggest that the observed ∼55 km transition depth identified by Jiang et al. (2024) does not represent a sharp shift in melting properties. Instead, it reflects a systematic filtering process: when the LAB depth is less than 55 km (corresponding to a minimum melting depth of ∼75 km after accounting for the gap between the top of the melting column and the LAB), pressures are low enough for all plumes to generate extensive melting. However, for lithosphere thicker than this threshold, plumes with lower melt fluxes generate insufficient melt volumes, effectively filtering themselves out as they are unlikely to drive surface volcanism. Comparison of simulations to observations suggests that a minimum melting degree of ∼2% represents a plausible threshold for melts to escape

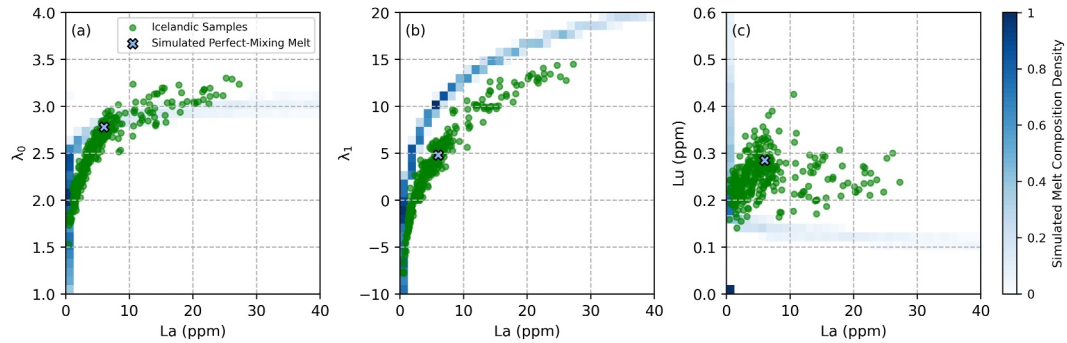

Figure 11. Predicted range of possible melt compositions within a single ocean island, compared to observations at Iceland. (a) λ_0 versus La (a light rare earth element) concentration. Blue squares = histogram of instantaneous melt compositions weighted by melt production rate for the ΔT400_LT15 simulation (chosen to be representative of Iceland) and a plume source composed of primitive mantle—darker blue areas indicate a higher volume of that simulated melt composition; blue cross = composition obtained by perfect homogenization of all instantaneous melts; green circles = observed Icelandic ocean island basalt samples following filtering and correction for fractional crystallization (Jiang et al., 2024). (b) Same for λ_1. (c) Same for Lu (a heavy rare earth element).

the mantle and erupt (Figure 10), aligning well with previous estimates (Schmeling, 2006; Sizova et al., 2015). While plume excess temperature is the primary control of melt flux in our simulations and is also expected to be the dominant variable on Earth, we note that plume size and source lithology may also play a role in influencing melt fluxes and the depth extent of melting.

Finally, a sampling bias in OIB databases may further reinforce the observational evidence for a *melt-flux filter*. Low-degree melts erupting through older, thicker lithosphere will likely form small-volume seamounts in deep water, making them less accessible for sampling and thus under-represented in global datasets.

4.2. Compositional Diversity of Melts Within a Single-Lithology Plume

Jiang et al. (2024) demonstrated a significant spread in observed OIB major element compositions that covary with both one another and trace elements, even for samples from the same ocean island and in places with thin lithosphere. For example, Icelandic basalts display a broad range of compositions, previously attributed to lithological heterogeneity in the melt source region and variations in magma evolution processes (e.g., Momme et al., 2003; Niu, 2021; Shorttle & Maclennan, 2011; Shorttle et al., 2014). However, Jiang et al. (2024) interpreted these trends as evidence that erupted basalts preserve high-pressure melting signatures from deeper parts of the melt domain, suggesting that melts from from different depths can reach the surface without extensive mixing and homogenization (e.g., Farnetani & Hofmann, 2010; Matthews et al., 2016; Sigmarsson & Steinthórsson, 2007). While variations in source lithology will produce a spread in major elements, it remains unclear how much of the observed compositional spread can be explained solely by melt sampling across the melting domain within a plume of a single lithology.

Although our coupled geochemical-geodynamical framework does not explicitly track variations in major element compositions of instantaneous melts, it allows us to assess trace element variability. To investigate this, we use the ΔT400_LT15 simulation at 6 Myr, which mimics melting conditions beneath Iceland. This case features a lithospheric thickness of ∼30 km and a maximum plume excess temperature just below the melting domain of $\Delta T_{pl} \approx 180$ K, consistent with observational estimates of Icelandic lithospheric thickness 20–30 km (e.g., Foulger et al., 2003; R. White et al., 1996) and plume excess temperature estimates of ∼160 K (e.g., Matthews et al., 2016; Shorttle et al., 2014; R. White et al., 1995).

Our results reveal that La concentrations exceed 35 ppm in the deepest melts and steadily decrease as melting progresses, eventually reaching zero (Figure 11). Across this deep-to-shallow melting sequence, λ_0 and λ_1 values also decrease from 3.0 to 1.0 and from 20 to −10, respectively. In contrast, Lu concentrations remain low and relatively stable in the deep melts formed within the garnet stability field, where Lu remains compatible. At shallower depths, within the spinel stability field, Lu concentrations begin to increase; however, by this stage, La has already been exhausted from the source. Ultimately, both La and Lu are depleted at the shallowest depths,

forming a cluster of melts in the simulation with negligible concentrations of either element. This depletion is represented as a dense, small patch in the lower-left corner of Figure 11c.

Although our simulations do not account for the subsequent processes of magma mixing, extraction and chamber evolution (e.g., Momme et al., 2003; Shorttle & Maclennan, 2011), the overall variability and distribution of instantaneous melts within the plume region are broadly consistent with observed Icelandic trace element chemistry (Figure 11). We also notice that observations do not display the most extreme values of La and Lu predicted in our simulations, which are likely associated with low volume melts from the very base and top of the melting region. These melts may experience some level of dilution by more voluminous melts from the central melting region, or become entrapped within the mantle.

Our findings suggest that much of the trace element diversity observed at single ocean islands, such as Iceland, can arise from local sampling of melts across the melting domain, even within a plume composed of a single lithology. Similar mechanisms of melt separation have been independently proposed to explain Icelandic (e.g., Nicholson & Latin, 1992) and Hawaiian OIB geochemistry (e.g., Farnetani & Hofmann, 2010; Sen et al., 2005). Furthermore, the observed compositional diversity indicates that melts from different depths do not undergo complete mixing. If mixing were fully efficient, the resulting compositions would converge toward the blue crosses in Figure 11, representing averaged melt compositions. Instead, our results support a scenario in which individual melts can preserve their depth-dependent geochemical signatures during ascent and eruption.

4.3. Evidence for a Recycled Component in the Plume Source

A recurring feature of our geochemical predictions, even when accounting for local melt sampling, is the underestimation of observed REE concentrations, particularly for HREEs (Figure 9a–9d). This discrepancy is difficult to reconcile with a source composed purely of primitive mantle, prompting consideration of variations in source composition. Geochemical observations (e.g., Chauvel et al., 2008; Halldórsson et al., 2016; Hofmann & White, 1982; Jackson et al., 2007; Shorttle & Maclennan, 2011; Shorttle et al., 2014; Sobolev et al., 2007; Weaver, 1991) and geodynamical models (e.g., Christensen & Hofmann, 1994; Jones et al., 2016, 2021; F. D. Richards et al., 2023) suggest that the OIB source region likely contains 2%–20% recycled material. Since recycled components are more trace-element enriched than primitive mantle peridotites (e.g., Kogiso et al., 1998), their incorporation would naturally elevate the trace element concentrations in plume-derived melts.

Our simulations do not capture multi-component melting under variable pressure-temperature conditions (e.g., Shorttle et al., 2014) or reactions between basaltic melts and surrounding peridotite to form pyroxenites (e.g., Kogiso et al., 1998; Mallik & Dasgupta, 2012; Nebel et al., 2019; Yaxley & Green, 1998). To explore the potential influence of source heterogeneity, we consider a simplified case in which we modify the trace element composition of our source by adding either 10 wt.% N-type basalts (S.-S. Sun & McDonough, 1989) or 20 wt.% gabbros (Niu & O'Hara, 2003) into the primitive mantle peridotite, without considering changes to the resulting mineral assemblage (Figure S9 in Supporting Information S1). Despite these simplifications, this approach yields an improved match between predicted and observed trace element concentrations while maintaining agreement with REE shape coefficients (Figures S10 and S11 in Supporting Information S1). Since basalts and gabbros have lower solidus temperatures than primitive mantle peridotite (Kogiso et al., 1998), they begin melting earlier, suggesting that our calculations likely provide an upper bound on the fraction of recycled material in the OIB source.

4.4. Melt Production Rates Versus Observed Eruptive Rates

The volumetric melt production rates of our simulations, ranging from 5×10^3 to 2×10^6 km^3 Myr^{-1}, encompass the observed eruptive rates for primary plumes, which are estimated at 10^4 to 10^5 km^3 Myr^{-1} (e.g., Duvernay et al., 2021; R. S. White, 1993). It is important to note that production rates represent an upper bound on eruptive rates, as some fraction of the generated melt does not reach the surface (e.g., Delaney & Pollard, 1982). For example, simulations with ΔT_{CMB} values of 400 and 500 K and initial lithospheric thicknesses of 56 and 95 km bracket the conditions expected for Hawaii. These cases produce peak excess temperatures beneath the melting region of 179–258 K and volumetric melt production rates consistent with independent estimates of magma generation (e.g., 1.4×10^5–3.5×10^5 km^3 Myr^{-1}; Farnetani & Hofmann, 2010; Robinson &

Eakins, 2006; R. S. White, 1993). The alignment of our simulated melt production rates with observed eruptive rates on Earth is both encouraging and supportive of the validity of our analyses.

4.5. Limitations and Uncertainties

In general, our simulation predictions are consistent with observed OIB trends, subject to the interpretations and caveats outlined in the previous sections. However, these results must be considered in the context of several limitations:

1. *Plume excess temperature and melt region geometry.* Our simulations assume an incompressible mantle and thus neglect adiabatic effects which cause temperature decreases during plume ascent (e.g., Leng & Zhong, 2008). A compressible mantle would also alter plume geometry, potentially impacting the shape of the melting region (Leng & Gurnis, 2012). Additionally, our initial conditions neglect non-adiabatic effects from internal heating. In an internally heated mantle, high upwelling velocities shorten the convective timescale relative to the ambient mantle, causing the plume to rise along a near-adiabatic gradient while the surrounding mantle undergoes non-adiabatic cooling. This reduces the temperature contrast between the plume and adjacent mantle, potentially modifying melting behavior (e.g., Bunge, 2005).
2. *Limitations in lithospheric and plate dynamics.* Our models face challenges in simulating thin lithosphere due to conductive thickening during plume stabilization, which restricts scenarios with lithospheric thicknesses below ∼40 km. Realistically capturing plume-lithosphere interactions in such settings would require incorporating mid-ocean ridge spreading. Additionally, our simulations neglect relative plate motion, meaning the plume continuously interacts with the same lithospheric region. In reality, plate motion significantly influences plume morphology and lithospheric thinning, leading to dynamic feedbacks (e.g., Cande & Stegman, 2011; Iaffaldano et al., 2018; Jones et al., 2017; Ribe & Christensen, 1999). For instance, the African plate remains relatively stationary in the hotspot reference frame, while the Pacific plate moves rapidly over the underlying mantle. Future studies should integrate tectonic motion to better capture the full range of plume-lithosphere interactions.
3. *Simulated plume buoyancy flux.* Our simulations produced buoyancy fluxes 2–3 times higher than observed estimates (e.g., Hoggard, Parnell-Turner, & White, 2020; King & Adam, 2014). Reducing the flux was challenging due to the need to obtain a critical thermal boundary layer thickness before plume ascent, which was difficult to modify within the constraints of our computationally expensive 3-D simulations. Tests using 2-D simulations indicate that shrinking Q_b by reducing the volumetric flux has minimal impact on geochemical trends, since the geometry and degree of melting remained largely unchanged (Figures S12 and S13 in Supporting Information S1), but does reduce both melt production rates and volumes. However, if Q_b is instead varied by changing plume excess temperature, both melt volumes and compositions are altered (since the degree of melting changes; Figure S14 in Supporting Information S1). Since our simulations yield realistic melt region excess temperatures and lithospheric thicknesses, these results imply that decreasing Q_b will likely preserve the simulated geochemical trends and only result in an equivalent reduction in melt production rates and volumes (i.e., the former scenario). As noted in our first limitation, fully compressible 3-D simulations, which account for the increase in plume excess temperatures with depth, are needed to confirm these findings.
4. *Focus on geochemical analyses at a specific time point.* We analyzed our simulations at 8 Myr after resetting of the lithospheric thermal structure (Section 3.1). However, plume fluxes vary over time (e.g., Lin & Van Keken, 2006), and our findings—based on a single snapshot—should be interpreted with these temporal fluctuations in mind.
5. *Uncertainties in rheological behavior.* The mechanical properties of the lithosphere and asthenosphere are critical in shaping plume evolution and lithosphere interaction (e.g., Burov & Guillou-Frottier, 2005; Burov et al., 2007; Sembroni et al., 2017; Wang & Li, 2021), but these properties are poorly constrained, introducing uncertainty into melting inferences.
6. *Lack of multi-component melting model to evaluate source variation.* By solely changing bulk element compositions, we found that incorporating recycled components into the source improves the match between predicted and observed trace element concentrations and REE shape coefficients. However, properly determining melt compositions for a source composed of mixed lithologies requires more sophisticated modeling and better petrological experimental constraints (e.g., Shorttle et al., 2014). Furthermore, we examined only fractional melting rather than batch melting, which may produce different F composition estimates (e.g., Plank et al., 1995).

7. *Absence of post-melting processes.* Our models do not account for processes such as melt movement (i.e., two-phase flow), reactive transport, magma mixing, tapping, crystallization, and recharge in crustal chambers (e.g., Borisova et al., 2017; Duvernay et al., 2024; Gleeson & Gibson, 2019). Since we compare our results to a fractionation-corrected OIB dataset (Jiang et al., 2024), our predictions are expected to closely approximate mantle-equilibrated compositions. However, these un-modeled processes likely introduce additional complexity to observed OIB chemistry.

5. Conclusions

We have used coupled geochemical-geodynamical simulations of peridotite melting in upwelling plumes to explore key geodynamic processes that shape observed trends in OIB geochemistry (Jiang et al., 2024).

First, our simulations support the role of a *lid effect*, where thicker lithosphere in older ocean basins acts as a mechanical barrier that limits the depth of shallow decompression melting. Additionally, they reveal a 10–30 km gap between the base of the lithospheric lid and the top of the melting region, formed as flow is redirected laterally beneath the LAB and cools. Simulation results also suggest that thermal rejuvenation of the lithosphere by a plume is more pronounced beneath thicker lithosphere and in the presence of hotter plumes.

Second, our simulations show that a *melt-flux filter*, whereby plumes with larger melt fluxes (primarily from higher excess temperatures) are preferentially sampled in thicker lithosphere, can explain the observed stabilization in melt fractions beyond a critical thickness of ∼55 km. Our results suggest that a minimum melting degree of ∼2% is required for successful melt extraction. This effect is further amplified by plume-driven lithospheric thinning, which becomes more effective with increasing lithospheric age.

Third, our simulations demonstrate that much of the observed trace element variability at individual ocean islands can be reproduced by local sampling of melts from across the melting domain, even in a single-lithology plume. This finding suggests that some high-pressure melts may ascend to the surface without being fully diluted by shallow melts, preserving deeper melting signatures in erupted basalts.

Finally, we find that observed REE concentrations in OIBs are consistently more enriched than predictions from a purely primitive mantle source. Incorporating a recycled oceanic component, either basalt or gabbro, improves the fit between model predictions and observations, supporting the idea that the OIB mantle source contains recycled crustal material.

In summary, these findings highlight the power of integrating geodynamic plume melting models with basalt geochemistry to investigate spatio-temporal variations in lithospheric architecture and mantle dynamics. The approach provides key insights into Earth's geodynamic evolution and mantle recycling processes, shedding light on earlier stages of the planet's history.

Acknowledgments
This research was undertaken with the assistance of resources from the *National Computational Infrastructure* (NCI Australia), a National Collaborative Research Infrastructure Strategy (NCRIS) enabled capability supported by the Australian Government, and was partially supported by the Australian Government through the *Australian Research Council's* Discovery Projects funding scheme (project DP200100053) and Discovery Early Career Researcher Awards (DE220101519). The authors are also grateful for funding provided by the *Chinese Scholarship Council* (CSC) scholarship and *Shen-su Sun* scholarship. Authors also acknowledge infrastructure support from AuScope, funded by the Australian Government through NCRIS. Open access publishing facilitated by Australian National University, as part of the Wiley - Australian National University agreement via the Council of Australian University Librarians.

Data Availability Statement

The Fluidity computational modeling framework is at https://fluidityproject.github.io, with the version used herein archived at (S. Kramer et al., 2023). Figures have been prepared using Matplotlib (Hunter, 2007) and PyVista (Sullivan & Kaszynski, 2019). OIB geochemistry data are compiled in Jiang (2024b). Simulation set-up files are stored in Zenodo (Jiang, 2024a).

References

Asimow, P. D., & Langmuir, C. (2003). The importance of water to oceanic mantle melting regimes. *Nature*, *421*(6925), 815–820. https://doi.org/10.1038/nature01429

Ball, P. W., Duvernay, T., & Davies, D. R. (2022). A coupled geochemical-geodynamic approach for predicting mantle melting in space and time. *Geochemistry, Geophysics, Geosystems*, *23*(4), e2022GC010421. https://doi.org/10.1029/2022gc010421

Ballmer, M. D., Ito, G., van Hunen, J., & Tackley, P. J. (2011). Spatial and temporal variability in Hawaiian hotspot volcanism induced by small-scale convection. *Nature Geoscience*, *4*(7), 457–460. https://doi.org/10.1038/ngeo1187

Bolfan-Casanova, N. (2005). Water in the Earth's mantle. *Mineralogical Magazine*, *69*(3), 229–257. https://doi.org/10.1180/0026461056930248

Borisova, A. Y., Bohrson, W. A., & Grégoire, M. (2017). Origin of primitive ocean island basalts by crustal gabbro assimilation and multiple recharge of plume-derived melts. *Geochemistry, Geophysics, Geosystems*, *18*(7), 2701–2716. https://doi.org/10.1002/2017gc006986

Brandenburg, J., Hauri, E. H., van Keken, P. E., & Ballentine, C. J. (2008). A multiple-system study of the geochemical evolution of the mantle with force-balanced plates and thermochemical effects. *Earth and Planetary Science Letters*, *276*(1–2), 1–13. https://doi.org/10.1016/j.epsl.2008.08.027

Bunge, H.-P. (2005). Low plume excess temperature and high core heat flux inferred from non-adiabatic geotherms in internally heated mantle circulation models. *Physics of the Earth and Planetary Interiors*, *153*(1–3), 3–10. https://doi.org/10.1016/j.pepi.2005.03.017

Burov, E., & Gerya, T. (2014). Asymmetric three-dimensional topography over mantle plumes. *Nature*, *513*(7516), 85–89. https://doi.org/10.1038/nature13703

Burov, E., & Guillou-Frottier, L. (2005). The plume head–continental lithosphere interaction using a tectonically realistic formulation for the lithosphere. *Geophysical Journal International*, *161*(2), 469–490. https://doi.org/10.1111/j.1365-246x.2005.02588.x

Burov, E., Guillou-Frottier, L., d'Acremont, E., Le Pourhiet, L., & Cloetingh, S. (2007). Plume head–lithosphere interactions near intra-continental plate boundaries. *Tectonophysics*, *434*(1–4), 15–38. https://doi.org/10.1016/j.tecto.2007.01.002

Campbell, I. H. (2007). Testing the plume theory. *Chemical Geology*, *241*(3–4), 153–176. https://doi.org/10.1016/j.chemgeo.2007.01.024

Campbell, I. H., Griffiths, R. W., & Hill, R. I. (1989). Melting in an Archaean mantle plume: Heads it's basalts, tails it's komatiites. *Nature*, *339*(6227), 697–699. https://doi.org/10.1038/339697a0

Cande, S. C., & Stegman, D. R. (2011). Indian and African plate motions driven by the push force of the Reunion plume head. *Nature*, *475*(7354), 47–52. https://doi.org/10.1038/nature10174

Chauvel, C., Lewin, E., Carpentier, M., Arndt, N. T., & Marini, J.-C. (2008). Role of recycled oceanic basalt and sediment in generating the Hf–Nd mantle array. *Nature Geoscience*, *1*(1), 64–67. https://doi.org/10.1038/ngeo.2007.51

Christensen, U. R., & Hofmann, A. W. (1994). Segregation of subducted oceanic crust in the convecting mantle. *Journal of Geophysical Research*, *99*(B10), 19867–19884. https://doi.org/10.1029/93jb03403

Crough, S. T. (1978). Thermal origin of mid-plate hot-spot swells. *Geophysical Journal International*, *55*(2), 451–469. https://doi.org/10.1111/j.1365-246x.1978.tb04282.x

Dannberg, J., & Sobolev, S. V. (2015). Low-buoyancy thermochemical plumes resolve controversy of classical mantle plume concept. *Nature Communications*, *6*(1), 6960. https://doi.org/10.1038/ncomms7960

Dasgupta, R., Jackson, M. G., & Lee, C.-T. A. (2010). Major element chemistry of ocean island basalts—Conditions of mantle melting and heterogeneity of mantle source. *Earth and Planetary Science Letters*, *289*(3–4), 377–392. https://doi.org/10.1016/j.epsl.2009.11.027

Davies, D. R., & Davies, J. H. (2009). Thermally-driven mantle plumes reconcile multiple hot-spot observations. *Earth and Planetary Science Letters*, *278*(1–2), 50–54. https://doi.org/10.1016/j.epsl.2008.11.027

Davies, D. R., Davies, J. H., Hassan, O., Morgan, K., & Nithiarasu, P. (2007). Investigations into the applicability of adaptive finite element methods to two-dimensional infinite Prandtl number thermal and thermochemical convection. *Geochemistry, Geophysics, Geosystems*, *8*(5), Q05010. https://doi.org/10.1029/2006gc001470

Davies, D. R., Goes, S., & Sambridge, M. (2015). On the relationship between volcanic hotspot locations, the reconstructed eruption sites of large igneous provinces and deep mantle seismic structure. *Earth and Planetary Science Letters*, *411*, 121–130. https://doi.org/10.1016/j.epsl.2014.11.052

Davies, D. R., Rawlinson, N., Iaffaldano, G., & Campbell, I. H. (2015). Lithospheric controls on magma composition along Earth's longest continental hotspot track. *Nature*, *525*(7570), 511–514. https://doi.org/10.1038/nature14903

Davies, D. R., Wilson, C. R., & Kramer, S. C. (2011). Fluidity: A fully unstructured anisotropic adaptive mesh computational modeling framework for geodynamics. *Geochemistry, Geophysics, Geosystems*, *12*(6), Q06001. https://doi.org/10.1029/2011gc003551

Delaney, P. T., & Pollard, D. D. (1982). Solidification of basaltic magma during flow in a dike. *American Journal of Science*, *282*(6), 856–885. https://doi.org/10.2475/ajs.282.6.856

Duncan, R. A., & Richards, M. A. (1991). Hotspots, mantle plumes, flood basalts, and true polar wander. *Reviews of Geophysics*, *29*(1), 31–50. https://doi.org/10.1029/90rg02372

Duvernay, T., Davies, D. R., Mathews, C. R., Gibson, A. H., & Kramer, S. C. (2021). Linking intraplate volcanism to lithospheric structure and asthenospheric flow. *Geochemistry, Geophysics, Geosystems*, *22*(8), e2021GC009953. https://doi.org/10.1029/2021gc009953

Duvernay, T., Davies, D. R., Mathews, C. R., Gibson, A. H., & Kramer, S. C. (2022). Continental magmatism: The surface manifestation of dynamic interactions between cratonic lithosphere, mantle plumes and edge-driven convection. *Geochemistry, Geophysics, Geosystems*, *23*(7), e2022GC010363. https://doi.org/10.1029/2022gc010363

Duvernay, T., Jiang, S., Ball, P. W., & Davies, D. R. (2024). Coupled geodynamical-geochemical perspectives on the generation and composition of mid-ocean ridge basalts. *Geochemistry, Geophysics, Geosystems*, *25*(2), e2023GC011288. https://doi.org/10.1029/2023gc011288

Ellam, R. (1992). Lithospheric thickness as a control on basalt geochemistry. *Geology*, *20*(2), 153–156. https://doi.org/10.1130/0091-7613(1992)020<0153:ltaaco>2.3.co;2

Farnetani, C. G., & Hofmann, A. W. (2010). Dynamics and internal structure of the Hawaiian plume. *Earth and Planetary Science Letters*, *295*(1–2), 231–240. https://doi.org/10.1016/j.epsl.2010.04.005

Farnetani, C. G., Hofmann, A. W., Duvernay, T., & Limare, A. (2018). Dynamics of rheological heterogeneities in mantle plumes. *Earth and Planetary Science Letters*, *499*, 74–82. https://doi.org/10.1016/j.epsl.2018.07.022

Foulger, G., Du, Z., & Julian, B. (2003). Icelandic-type crust. *Geophysical Journal International*, *155*(2), 567–590. https://doi.org/10.1046/j.1365-246x.2003.02056.x

French, S. W., & Romanowicz, B. (2015). Broad plumes rooted at the base of the Earth's mantle beneath major hotspots. *Nature*, *525*(7567), 95–99. https://doi.org/10.1038/nature14876

Garel, F., Goes, S., Davies, D. R., Davies, J. H., Kramer, S. C., & Wilson, C. R. (2014). Interaction of subducted slabs with the mantle transition-zone: A regime diagram from 2-D thermo-mechanical models with a mobile trench and an overriding plate. *Geochemistry, Geophysics, Geosystems*, *15*(5), 1739–1765. https://doi.org/10.1002/2014gc005257

Gibson, S., & Geist, D. (2010). Geochemical and geophysical estimates of lithospheric thickness variation beneath galápagos. *Earth and Planetary Science Letters*, *300*(3–4), 275–286. https://doi.org/10.1016/j.epsl.2010.10.002

Gleeson, M. L., & Gibson, S. A. (2019). Crustal controls on apparent mantle pyroxenite signals in ocean-island basalts. *Geology*, *47*(4), 321–324. https://doi.org/10.1130/g45759.1

Griffiths, R. W., & Campbell, I. H. (1990). Stirring and structure in mantle starting plumes. *Earth and Planetary Science Letters*, *99*(1–2), 66–78. https://doi.org/10.1016/0012-821x(90)90071-5

Griffiths, R. W., & Campbell, I. H. (1991). On the dynamics of long-lived plume conduits in the convecting mantle. *Earth and Planetary Science Letters*, *103*(1–4), 214–227. https://doi.org/10.1016/0012-821x(91)90162-b

Hager, B. H., Clayton, R. W., Richards, M. A., Comer, R. P., & Dziewonski, A. M. (1985). Lower mantle heterogeneity, dynamic topography and the geoid. *Nature*, *313*(6003), 541–545. https://doi.org/10.1038/313541a0

Halldórsson, S. A., Barnes, J. D., Stefánsson, A., Hilton, D. R., Hauri, E. H., & Marshall, E. W. (2016). Subducted lithosphere controls halogen enrichments in the Iceland mantle plume source. *Geology*, *44*(8), 679–682. https://doi.org/10.1130/g37924.1

Hofmann, A. W., & White, W. M. (1982). Mantle plumes from ancient oceanic crust. *Earth and Planetary Science Letters*, *57*(2), 421–436. https://doi.org/10.1016/0012-821x(82)90161-3
Hoggard, M. J., Czarnota, K., Richards, F. D., Huston, D. L., Jaques, A. L., & Ghelichkhan, S. (2020). Global distribution of sediment-hosted metals controlled by craton edge stability. *Nature Geoscience*, *13*(7), 504–510. https://doi.org/10.1038/s41561-020-0593-2
Hoggard, M. J., Parnell-Turner, R., & White, N. (2020). Hotspots and mantle plumes revisited: Towards reconciling the mantle heat transfer discrepancy. *Earth and Planetary Science Letters*, *542*, 116317. https://doi.org/10.1016/j.epsl.2020.116317
Hole, M. J., & Millett, J. (2016). Controls of mantle potential temperature and lithospheric thickness on magmatism in the North Atlantic Igneous Province. *Journal of Petrology*, *57*(2), 417–436. https://doi.org/10.1093/petrology/egw014
Humphreys, E. R., & Niu, Y. (2009). On the composition of ocean island basalts (OIB): The effects of lithospheric thickness variation and mantle metasomatism. *Lithos*, *112*(1–2), 118–136. https://doi.org/10.1016/j.lithos.2009.04.038
Hunter, J. D. (2007). Matplotlib: A 2D graphics environment. *Computer Science and Engineering*, *9*(3), 90–95. https://doi.org/10.1109/MCSE.2007.55
Iaffaldano, G., Davies, D. R., & DeMets, C. (2018). Indian Ocean floor deformation induced by the Reunion plume rather than the Tibetan Plateau. *Nature Geoscience*, *11*(5), 362–366. https://doi.org/10.1038/s41561-018-0110-z
Jackson, M. G., Hart, S. R., Koppers, A. A., Staudigel, H., Konter, J., Blusztajn, J., et al. (2007). The return of subducted continental crust in Samoan lavas. *Nature*, *448*(7154), 684–687. https://doi.org/10.1038/nature06048
Jiang, S. (2024a). Geodynamical simulations of mantle plume melting [Dataset]. *Zenodo*. https://doi.org/10.5281/zenodo.14319838
Jiang, S. (2024b). OIB Geochemistry & Lithospheric Thickness [Dataset]. *Zenodo*. https://doi.org/10.5281/zenodo.10889440
Jiang, S., Hawkins, R., Hoggard, M. J., Davies, D. R., & Campbell, I. H. (2024). Investigating the lid effect on the generation of ocean island basalts: 1. Geochemical trends. *Geochemistry, Geophysics, Geosystems*, *25*(6), e2023GC011387. https://doi.org/10.1029/2023gc011387
Jones, T. D., Davies, D. R., Campbell, I. H., Iaffaldano, G., Yaxley, G. M., Kramer, S. C., & Wilson, C. R. (2017). The concurrent emergence and causes of double volcanic hotspot tracks on the Pacific plate. *Nature*, *545*(7655), 472–476. https://doi.org/10.1038/nature22054
Jones, T. D., Davies, D. R., Campbell, I. H., Wilson, C. R., & Kramer, S. C. (2016). Do mantle plumes preserve the heterogeneous structure of their deep-mantle source? *Earth and Planetary Science Letters*, *434*, 10–17. https://doi.org/10.1016/j.epsl.2015.11.016
Jones, T. D., Davies, D. R., & Sossi, P. A. (2019). Tungsten isotopes in mantle plumes: Heads it's positive, tails it's negative. *Earth and Planetary Science Letters*, *506*, 255–267. https://doi.org/10.1016/j.epsl.2018.11.008
Jones, T. D., Sime, N., & Van Keken, P. E. (2021). Burying Earth's primitive mantle in the slab graveyard. *Geochemistry, Geophysics, Geosystems*, *22*(3), e2020GC009396. https://doi.org/10.1029/2020gc009396
Keller, T., Katz, R. F., & Hirschmann, M. M. (2017). Volatiles beneath mid-ocean ridges: Deep melting, channelised transport, focusing, and metasomatism. *Earth and Planetary Science Letters*, *464*, 55–68. https://doi.org/10.1016/j.epsl.2017.02.006
King, S. D., & Adam, C. (2014). Hotspot swells revisited. *Physics of the Earth and Planetary Interiors*, *235*, 66–83. https://doi.org/10.1016/j.pepi.2014.07.006
Kogiso, T., Hirose, K., & Takahashi, E. (1998). Melting experiments on homogeneous mixtures of peridotite and basalt: Application to the genesis of ocean island basalts. *Earth and Planetary Science Letters*, *162*(1–4), 45–61. https://doi.org/10.1016/s0012-821x(98)00156-3
Koppers, A. A., Becker, T. W., Jackson, M. G., Konrad, K., Müller, R. D., Romanowicz, B., et al. (2021). Mantle plumes and their role in Earth processes. *Nature Reviews Earth & Environment*, *2*(6), 382–401. https://doi.org/10.1038/s43017-021-00168-6
Kramer, S., Greaves, T., Funke, S. W., Wilson, C., Avdis, A., Davies, R., et al. (2023). FluidityProject/fluidity: Zenodo release [Dataset]. *Zenodo*. https://doi.org/10.5281/zenodo.8268830
Kramer, S. C., Davies, D. R., & Wilson, C. R. (2021). Analytical solutions for mantle flow in cylindrical and spherical shells. *Geoscientific Model Development*, *14*(4), 1899–1919. https://doi.org/10.5194/gmd-14-1899-2021
Kramer, S. C., Wilson, C. R., & Davies, D. R. (2012). An implicit free surface algorithm for geodynamical simulations. *Physics of the Earth and Planetary Interiors*, *194*, 25–37. https://doi.org/10.1016/j.pepi.2012.01.001
Leng, W., & Gurnis, M. (2012). Shape of thermal plumes in a compressible mantle with depth-dependent viscosity. *Geophysical Research Letters*, *39*(5), L05310. https://doi.org/10.1029/2012gl050959
Leng, W., & Zhong, S. (2008). Controls on plume heat flux and plume excess temperature. *Journal of Geophysical Research*, *113*(B4), B04408. https://doi.org/10.1029/2007jb005155
Le Voci, G., Davies, D. R., Goes, S., Kramer, S. C., & Wilson, C. R. (2014). A systematic 2-D investigation into the mantle wedge's transient flow regime and thermal structure: Complexities arising from a hydrated rheology and thermal buoyancy. *Geochemistry, Geophysics, Geosystems*, *15*(1), 28–51. https://doi.org/10.1002/2013gc005022
Li, X., Kind, R., Yuan, X., Wölbern, I., & Hanka, W. (2004). Rejuvenation of the lithosphere by the Hawaiian plume. *Nature*, *427*(6977), 827–829. https://doi.org/10.1038/nature02349
Lin, S.-C., & van Keken, P. E. (2005). Multiple volcanic episodes of flood basalts caused by thermochemical mantle plumes. *Nature*, *436*(7048), 250–252. https://doi.org/10.1038/nature03697
Lin, S.-C., & Van Keken, P. E. (2006). Dynamics of thermochemical plumes: 2. Complexity of plume structures and its implications for mapping mantle plumes. *Geochemistry, Geophysics, Geosystems*, *7*(3), Q03003. https://doi.org/10.1029/2005gc001072
Mallik, A., & Dasgupta, R. (2012). Reaction between MORB-eclogite derived melts and fertile peridotite and generation of ocean island basalts. *Earth and Planetary Science Letters*, *329*, 97–108. https://doi.org/10.1016/j.epsl.2012.02.007
Mathews, C. (2021). *Methods for tracking material properties within an unstructured, adaptive mesh computational modelling framework, with application to simulating the development of seismic anisotropy at spreading centres and transform faults* (Unpublished doctoral dissertation). The Australian National University.
Matthews, S., Shorttle, O., & Maclennan, J. (2016). The temperature of the Icelandic mantle from olivine-spinel aluminum exchange thermometry. *Geochemistry, Geophysics, Geosystems*, *17*(11), 4725–4752. https://doi.org/10.1002/2016gc006497
McKenzie, D. (1984). The generation and compaction of partially molten rock. *Journal of Petrology*, *25*(3), 713–765. https://doi.org/10.1093/petrology/25.3.713
McKenzie, D., & Bickle, M. (1988). The volume and composition of melt generated by extension of the lithosphere. *Journal of Petrology*, *29*(3), 625–679. https://doi.org/10.1093/petrology/29.3.625
Momme, P., Óskarsson, N., & Keays, R. R. (2003). Platinum-group elements in the Icelandic rift system: Melting processes and mantle sources beneath Iceland. *Chemical Geology*, *196*(1–4), 209–234.
Morgan, W. J. (1971). Convection plumes in the lower mantle. *Nature*, *230*(5288), 42–43. https://doi.org/10.1038/230042a0
Nakada, M., Okuno, J., & Irie, Y. (2018). Inference of viscosity jump at 670 km depth and lower mantle viscosity structure from GIA observations. *Geophysical Journal International*, *212*(3), 2206–2225. https://doi.org/10.1093/gji/ggx519

Nebel, O., Sossi, P. A., Bénard, A., Arculus, R. J., Yaxley, G. M., Woodhead, J. D., et al. (2019). Reconciling petrological and isotopic mixing mechanisms in the Pitcairn mantle plume using stable Fe isotopes. *Earth and Planetary Science Letters*, *521*, 60–67. https://doi.org/10.1016/j.epsl.2019.05.037

Nicholson, H., & Latin, D. (1992). Olivine tholeiites from Krafla, Iceland: Evidence for variations in melt fraction within a plume. *Journal of Petrology*, *33*(5), 1105–1124. https://doi.org/10.1093/petrology/33.5.1105

Niu, Y. (2021). Lithosphere thickness controls the extent of mantle melting, depth of melt extraction and basalt compositions in all tectonic settings on Earth – A review and new perspectives. *Earth-Science Reviews*, *217*, 103614. https://doi.org/10.1016/j.earscirev.2021.103614

Niu, Y., & O'Hara, M. J. (2003). Origin of ocean island basalts: A new perspective from petrology, geochemistry, and mineral physics considerations. *Journal of Geophysical Research*, *108*(B4), 2209. https://doi.org/10.1029/2002jb002048

Niu, Y., Wilson, M., Humphreys, E. R., & O'Hara, M. J. (2011). The origin of intra-plate ocean island basalts (OIB): The lid effect and its geodynamic implications. *Journal of Petrology*, *52*(7–8), 1443–1468. https://doi.org/10.1093/petrology/egr030

O'Neill, H. S. C. (2016). The smoothness and shapes of chondrite-normalized rare earth element patterns in basalts. *Journal of Petrology*, *57*(8), 1463–1508. https://doi.org/10.1093/petrology/egw047

Plank, T., Spiegelman, M., Langmuir, C. H., & Forsyth, D. W. (1995). The meaning of "mean F": Clarifying the mean extent of melting at ocean ridges. *Journal of Geophysical Research*, *100*(B8), 15045–15052. https://doi.org/10.1029/95jb01148

Ribe, N., & Christensen, U. R. (1999). The dynamical origin of Hawaiian volcanism. *Earth and Planetary Science Letters*, *171*(4), 517–531. https://doi.org/10.1016/s0012-821x(99)00179-x

Richards, F. D., Hoggard, M. J., Crosby, A., Ghelichkhan, S., & White, N. (2020). Structure and dynamics of the oceanic lithosphere-asthenosphere system. *Physics of the Earth and Planetary Interiors*, *309*, 106559. https://doi.org/10.1016/j.pepi.2020.106559

Richards, F. D., Hoggard, M. J., Ghelichkhan, S., Koelemeijer, P., & Lau, H. C. (2023). Geodynamic, geodetic, and seismic constraints favour deflated and dense-cored LLVPs. *Earth and Planetary Science Letters*, *602*, 117964. https://doi.org/10.1016/j.epsl.2022.117964

Richards, F. D., Hoggard, M. J., White, N., & Ghelichkhan, S. (2020). Quantifying the relationship between short-wavelength dynamic topography and thermomechanical structure of the upper mantle using calibrated parameterization of an elasticity. *Journal of Geophysical Research: Solid Earth*, *125*(9), e2019JB019062. https://doi.org/10.1029/2019jb019062

Richards, M. A., Duncan, R. A., & Courtillot, V. E. (1989). Flood basalts and hot-spot tracks: Plume heads and tails. *Science*, *246*(4926), 103–107. https://doi.org/10.1126/science.246.4926.103

Robinson, J. E., & Eakins, B. W. (2006). Calculated volumes of individual shield volcanoes at the young end of the Hawaiian Ridge. *Journal of Volcanology and Geothermal Research*, *151*(1–3), 309–317. https://doi.org/10.1016/j.jvolgeores.2005.07.033

Schmeling, H. (2006). A model of episodic melt extraction for plumes. *Journal of Geophysical Research*, *111*(B3), B03202. https://doi.org/10.1029/2004jb003423

Sembroni, A., Kiraly, A., Faccenna, C., Funiciello, F., Becker, T. W., Globig, J., & Fernandez, M. (2017). Impact of the lithosphere on dynamic topography: Insights from analogue modeling. *Geophysical Research Letters*, *44*(6), 2693–2702. https://doi.org/10.1002/2017gl072668

Sen, G., Keshav, S., & Bizimis, M. (2005). Hawaiian mantle xenoliths and magmas: Composition and thermal character of the lithosphere. *American Mineralogist*, *90*(5–6), 871–887.

Shaw, D. M. (1979). Trace element melting models. *Physics and Chemistry of the Earth*, *11*, 577–586. https://doi.org/10.1016/0079-1946(79)90055-7

Shorttle, O., & Maclennan, J. (2011). Compositional trends of Icelandic basalts: Implications for short–length scale lithological heterogeneity in mantle plumes. *Geochemistry, Geophysics, Geosystems*, *12*(11), Q11008. https://doi.org/10.1029/2011gc003748

Shorttle, O., Maclennan, J., & Lambart, S. (2014). Quantifying lithological variability in the mantle. *Earth and Planetary Science Letters*, *395*, 24–40. https://doi.org/10.1016/j.epsl.2014.03.040

Sigmarsson, O., & Steinthórsson, S. (2007). Origin of Icelandic basalts: A review of their petrology and geochemistry. *Journal of Geodynamics*, *43*(1), 87–100. https://doi.org/10.1016/j.jog.2006.09.016

Sim, S. J., Spiegelman, M., Stegman, D. R., & Wilson, C. (2020). The influence of spreading rate and permeability on melt focusing beneath mid-ocean ridges. *Physics of the Earth and Planetary Interiors*, *304*, 106486. https://doi.org/10.1016/j.pepi.2020.106486

Sizova, E., Gerya, T., Stüwe, K., & Brown, M. (2015). Generation of felsic crust in the Archean: A geodynamic modeling perspective. *Precambrian Research*, *271*, 198–224. https://doi.org/10.1016/j.precamres.2015.10.005

Sleep, N. H. (1990). Hotspots and mantle plumes: Some phenomenology. *Journal of Geophysical Research*, *95*(B5), 6715–6736. https://doi.org/10.1029/jb095ib05p06715

Sleep, N. H. (2006). Mantle plumes from top to bottom. *Earth-Science Reviews*, *77*(4), 231–271. https://doi.org/10.1016/j.earscirev.2006.03.007

Sobolev, A. V., Hofmann, A. W., Kuzmin, D. V., Yaxley, G. M., Arndt, N. T., Chung, S.-L., et al. (2007). The amount of recycled crust in sources of mantle-derived melts. *Science*, *316*(5823), 412–417. https://doi.org/10.1126/science.1138113

Soderman, C. R., Matthews, S., Shorttle, O., Jackson, M. G., Day, J. M., Kamenetsky, V., & Williams, H. M. (2024). Global oceanic basalt sources and processes viewed through combined Fe and Mg stable isotopes. *Earth and Planetary Science Letters*, *638*, 118749. https://doi.org/10.1016/j.epsl.2024.118749

Sullivan, C. B., & Kaszynski, A. (2019). PyVista: 3D plotting and mesh analysis through a streamlined interface for the Visualization Toolkit (VTK). *Journal of Open Source Software*, *4*(37), 1450. https://doi.org/10.21105/joss.01450

Sun, C., & Liang, Y. (2013). The importance of crystal chemistry on REE partitioning between mantle minerals (garnet, clinopyroxene, orthopyroxene, and olivine) and basaltic melts. *Chemical Geology*, *358*, 23–36. https://doi.org/10.1016/j.chemgeo.2013.08.045

Sun, S.-S., & McDonough, W. F. (1989). Chemical and isotopic systematics of oceanic basalts: Implications for mantle composition and processes. *Geological Society - Special Publications*, *42*(1), 313–345. https://doi.org/10.1144/gsl.sp.1989.042.01.19

Tosi, N., Stein, C., Noack, L., Hüttig, C., Maierova, P., Samuel, H., et al. (2015). A community benchmark for viscoplastic thermal convection in a 2-D square box. *Geochemistry, Geophysics, Geosystems*, *16*(7), 2175–2196. https://doi.org/10.1002/2015gc005807

Wallace, P. J. (1998). Water and partial melting in mantle plumes: Inferences from the dissolved H_2O concentrations of Hawaiian basaltic magmas. *Geophysical Research Letters*, *25*(19), 3639–3642. https://doi.org/10.1029/98gl02805

Wang, Y., & Li, M. (2021). The interaction between mantle plumes and lithosphere and its surface expressions: 3-D numerical modelling. *Geophysical Journal International*, *225*(2), 906–925. https://doi.org/10.1093/gji/ggab014

Watson, S., & McKenzie, D. (1991). Melt generation by plumes: A study of Hawaiian volcanism. *Journal of Petrology*, *32*(3), 501–537. https://doi.org/10.1093/petrology/32.3.501

Weaver, B. L. (1991). Trace element evidence for the origin of ocean-island basalts. *Geology*, *19*(2), 123–126. https://doi.org/10.1130/0091-7613(1991)019<0123:teefto>2.3.co;2

White, R., Bown, J., & Smallwood, J. (1995). The temperature of the Iceland plume and origin of outward-propagating V-shaped ridges. *Journal of the Geological Society*, *152*(6), 1039–1045. https://doi.org/10.1144/gsl.jgs.1995.152.01.26

White, R., & McKenzie, D. (1989). Magmatism at rift zones: The generation of volcanic continental margins and flood basalts. *Journal of Geophysical Research*, *94*(B6), 7685–7729. https://doi.org/10.1029/jb094ib06p07685

White, R., Minshull, T., Richardson, K., Smallwood, J., Staples, R., McBride, J., et al. (1996). Seismic images of crust beneath Iceland contribute to long-standing debate. *Eos, Transactions American Geophysical Union*, *77*(21), 197–201. https://doi.org/10.1029/96eo00134

White, R. S. (1993). Melt production rates in mantle plumes. *Philosophical Transactions of the Royal Society of London - A*, *342*(1663), 137–153.

White, R. S., McKenzie, D., & O'Nions, R. K. (1992). Oceanic crustal thickness from seismic measurements and rare earth element inversions. *Journal of Geophysical Research*, *97*(B13), 19683–19715. https://doi.org/10.1029/92jb01749

Wilson, C. (2009). *Modelling multiple-material flows on adaptive unstructured meshes* (Unpublished doctoral dissertation). Imperial College London.

Wood, B., & Blundy, J. (2014). 3.11-Trace element partitioning: The influences of ionic radius, cation charge, pressure, and temperature. *Treatise on Geochemistry*, 421–448.

Yaxley, G. M., & Green, D. H. (1998). Reactions between eclogite and peridotite: Mantle refertilisation by subduction of oceanic crust. *Schweizerische Mineralogische und Petrographische Mitteilungen*, *78*(2), 243–255.